STUDY OF TWO-DIMENSIONAL CALCULATION OF CRATERING

PIFR-032

by Donald E. Maxwell, Ronald Hofmann, Dudley J. Andrews, and Ernest T. Trigg

June 30, 1966

prepared for
National Aeronautics and Space Administration
Goddard Space Flight Center
Greenbelt, Maryland
under Contract NAS5-9202

Physics International Company
2700 Merced Street
San Leandro, California 94677

CONTENTS

LIST OF ILLUSTRATIONS

SECTION I

INTRODUCTION

Physics International has developed the capability of solving a class of problems known as "cratering" calculations. Three problems, each dealing with a different facet of cratering phenomena, have recently been completed under Contract NAS5-9202 for the National Aeronautics and Space Administration. The first problem involved the simulation of the DANNY BOY nuclear cratering experiment and was an example of an "explosive" type of cratering problem. The second problem dealt with the crater formed by an aluminum sphere impacting an aluminum half space; it may be referred to as an "impact" type of cratering problem. The third problem dealt with another impact situation and calculated the trajectories of ejecta emitted from a large comet impacting the surface of the earth.

The capability to calculate cratering has been created primarily by the completion of various new options and modifications to Physics International's ELK code (a two-dimensional, Eulerian-Lagrangian coupled code). The most important of the modifications is a new formulation for the energy difference equations in the Eulerian region that conserves total energy. Cumulative errors resulting in as much as 20 to 40 per cent energy loss during the initial violent expansion have been eliminated. A second modification is a "dezoning" scheme for the Eulerian grid. One new option makes it possible to attach the Lagrangian grid only when necessary, and a second makes it possible to discard the Euler grid when it is no longer important. These features have helped make the ELK code an efficient "system" for doing cratering problems.

In addition to the increased code capabilities, advances have been made in describing the strength of granular materials. A Mohr-Coulomb yield strength model has been developed and was used in the DANNY BOY problem. Also some exploratory experiment and computation has been undertaken to gain some insight into the equations of state of porous media.

Associated with this work codes to assimilate and correlate Hugoniot data are being formulated in order to contribute to the development of an up-to-date library of equations of state and material properties.

This report first describes the characteristics of the ELK code and then presents the results of the three problems calculated.

SECTION II

DEVELOPMENT OF A CRATERING CALCULATION CAPABILITY

A. THE COMPUTATIONAL CODE, ELK

ELK is a two-dimensional, time-dependent, coupled Eulerian-Lagrangian code designed specifically for cratering calculations (Ref. 1). The coupling at the interface between the Eulerian and the Lagrangian regions is accomplished using the method developed by W. F. Noh (Ref. 2) for his CEL code.

For a typical "explosive" cratering problem, the source and a portion of the earth near it are included in the Eulerian region. At larger distances the Euler grid is covered by the Lagrange grid. As time progresses, the interface boundary, which is a line of the Lagrange grid, moves outward with the velocity of the material and uncovers new Euler cells. Cells of the Euler grid that are partly uncovered are hybrid, in that there is flow through the exposed portions of the Euler grid together with the motion of the Lagrange interface. The formulation of the equations for such interface cells is essential to the coupling.

The calculation in the Lagrangian region is the same as that in PIPE (Physics International's two-dimensional, elastic-plastic Lagrangian code, Ref. 3). Elastic-plastic properties of real materials are taken into account. A more complete description of solid properties is possible in a Lagrangian code, thus making it feasible to carry the calculation to later times and perhaps to investigate the final stages of crater formation.

The calculations made for each step in problem time consist of four main parts: Lagrange calculations, Euler calculations, and two phases of coupling. At the beginning of a cycle, the known state of the Lagrange material and the pressure acting on its interface boundary are used to advance through time all the Lagrange

variables. Next, the new position of the Lagrange interface boundary is used to determine the new volume of the Euler interface cells. Then the Euler variables may be advanced in time. Finally, from the Eulerian solution, the second phase of the coupling calculation determines the new pressure that acts on the interface boundary of the Lagrange grid.

1. Special Features of the ELK Code

The ELK code is really several codes in one. It is possible to run with an Euler grid alone, a Lagrange grid alone, or with both grids coupled in one configuration. It is possible to stop any of these runs at any time and later restart them from information automatically stored on a "restart tape." Altogether there are eight distinct kinds of runs that can be made.

In particular it is possible to (1) dezone a pure Euler run at any time, (2) use the output from a pure Euler run as input to a coupled run, and (3) use the output from a coupled run as input to a pure Lagrange run.

Using only input cards, initial values of variables of both grids can be specified in a very general way. Up to ten different regions of initial values can be defined in either grid. These regions can be independently specified in a variety of ways; e.g., circles, squares, etc. Using a similar scheme, regions of either grid can be arbitrarily redefined at "restart time." This last feature can be particularly useful if a run has gotten into trouble and the "trouble" can be arbitrarily eliminated without affecting the usefulness of the run.

The code may run using either axial symmetry or translational (slab) symmetry. Gravity is also available, if desired.

Every zone in the Lagrange grid has a "material number" associated with it. Among other things, this means that different

parts of the grid can have different equations of state. Up to ten distinct materials may be used.

The boundary conditions imposed on the four boundaries of the Euler grid can be specified in a very general way. The options available are (1) sliding on a fixed boundary, (2) input of fluid at a prescribed velocity, and (3) an approximate escape condition. These options exist in addition to the standard fixed and free boundary options.

2. Dezoning

While running the pure Eulerian part of the ELK code, it is possible to "dezone" the entire Euler grid at any time and continue the run. Often this means that a run that would take many hours without dezoning can be done in a small fraction of the time.

The Euler grid contains the same number of cells before and after dezoning. It is only the dimensions of the grid that are changed. When dezoning, each cell in the Euler grid--and hence the grid as a whole--is doubled in size. Each new mass cell that lies on top of the old grid will contain the material that had been in four old mass cells. Each new mass cell that lies outside the old grid is initialized to the undisturbed values of the appropriate material. A volume-weighted average of each variable for each set of four old mass cells is used to accurately define variables in one new, dezoned mass cell. The situation for momentum cells is somewhat more complicated because some old momentum cells are distributed among several new, dezoned momentum cells; but the principle is exactly the same.

When using dezoning, the usual procedure is to run a problem until activity is close to the boundaries of the current Euler grid. The problem is stopped, then dezoned and restarted in the new Euler grid. It is run until activity again approaches the boundaries and then dezoned again if desired. The run can go through as many dezone stages as desired. After the last run in such a series, the Euler grid still

contains the original number of cells. However, all linear dimensions are scaled by a factor of 2^n, where n is the number of dezones used.

At any point during a pure Eulerian run, before or after dezoning, the restart tape produced by the last run can be used as input to the coupled configuration. At this point the Lagrange grid must be defined by input cards; however, the Euler grid is completely specified by the restart tape from the pure Eulerian run.

3. New Energy Equations

Within the past year it was discovered that a pure Eulerian calculation done at Physics International disagreed with an equivalent calculation done at General Atomics on their OIL code (Ref. 4). Further calculations on a problem with a known solution revealed that, under conditions of relatively coarse zoning and high energy density, the total energy in the problem was not conserved resulting in a degradation of peak stresses and velocities. The discrepancy was corrected by calculating total energy density explicitly, rather than internal energy density. The discussion of this change will start with a statement of the relevant differential equations.

Let I be internal energy per unit volume, T be kinetic energy per unit volume, and W be total energy per unit volume.

Then $$W = I + T$$

The differential equation for internal energy density in Eulerian coordinates is

$$\frac{\partial I}{\partial t} + \vec{\nabla} \cdot (I\vec{u}) = - (P + Q) \vec{\nabla} \cdot \vec{u} \qquad (1)$$

where P is pressure and Q the contribution to pressure from artificial viscosity. The term on the right side is the rate at which thermodynamic work is done per unit volume, $-(P + Q) \frac{1}{V} \frac{\partial V}{\partial t}$.

The differential equation for kinetic energy density is

$$\frac{\partial T}{\partial t} + \vec{\nabla} \cdot (T\vec{u}) = - \vec{\nabla}(P + Q) \cdot \vec{u} \qquad (2)$$

where the term on the right side is the force per unit volume times velocity, or the power per unit volume for the special case of incompressible motion.

The sum of Equations (1) and (2) is

$$\frac{\partial(I + T)}{\partial t} + \vec{\nabla} \cdot \left[(I + T)\vec{u}\right] = -(P + Q)\vec{\nabla} \cdot \vec{u} - \vec{u} \cdot \vec{\nabla}(P + Q)$$

or

$$\frac{\partial W}{\partial t} + \vec{\nabla} \cdot \left[W\vec{u}\right] = -\vec{\nabla} \cdot \left[(P + Q)\vec{u}\right]$$

which may be rearranged as

$$\frac{\partial W}{\partial t} = -\vec{\nabla} \cdot \left[(W + P + Q)\vec{u}\right] \qquad (3)$$

This equation states that the rate of change of total energy density is the rate of transport of the quantity $(W + P + Q)$, which coincidentally, may be recognized as the quantity that appears in Bernoulli's law.

Physics International's Eulerian code, FLU, formerly used a finite difference analog of Equation (1) (W. F. Noh's original version, Ref. 2) to calculate internal energy density. The resulting system of equations did not conserve total energy exactly. The reason is that as diffusion takes place, the momentum in the problem is distributed over a larger mass, and the kinetic energy decreases. In other words, the finite difference analog of Equation (2) is not implied by the equations for momentum and mass conservation without significant truncation errors. The error was worst in the case of large velocity gradients and coarse zoning.

The most direct way to achieve conservation of energy is to use a finite difference analog of Equation (3). Applying Noh's general finite-difference formula for a transport term to the right side of Equation (3), the conservation is exact. As in the case of all the transport terms, the equation is not correctly time centered, for the quantity transported is taken from the previous time step. The lack of time centering is partly compensated for by setting the value of the quantity at a cell face equal

to its value in the upstream cell. Since the work now appears as part of a transport term, the new energy depends on old pressures. Therefore the usual iteration between the equations for pressure and energy may be eliminated, while preserving the same order of accuracy used in the other equations.

The total energy density, when calculated as discussed above, is most naturally defined in mass cells at integral time steps. The internal energy density may be obtained from the equation

$$I = W - T$$

where the kinetic energy density T is determined by the momentum equations uniquely for a continuum. In the finite difference case, however, T may be defined in several different ways, since mass and velocity are defined at different points in space and also at different points in time, and several different averaging procedures are possible.

To test various sets of finite-difference equations that conserve total energy precisely, a one-dimensional version of the pure Eulerian code was used. The test problem used was the impact of a plate on a target that was a gamma-law gas. An analytic solution for this problem is known. In each case the problem was run until the peak pressure decayed two orders of magnitude. In Figure 1, pressure is plotted against distance at this time. The solid curve is the analytic solution. The circled points are from the old equations in which energy is not conserved. The peak pressure is too low, and the shock front is lagging behind the correct position. It was found that all variations of the equations that conserve total energy gave a significant improvement. Results from the version that was finally chosen are shown in the figure. Near the peak, a point is plotted from each zone. The definition that is obtained is as good as one could hope for.

With the new equations it is not necessary to use an artificial viscosity when calculating a strong shock moving into a gamma-law gas at rest. In other situations, however, the artificial viscosity may be necessary or desirable.

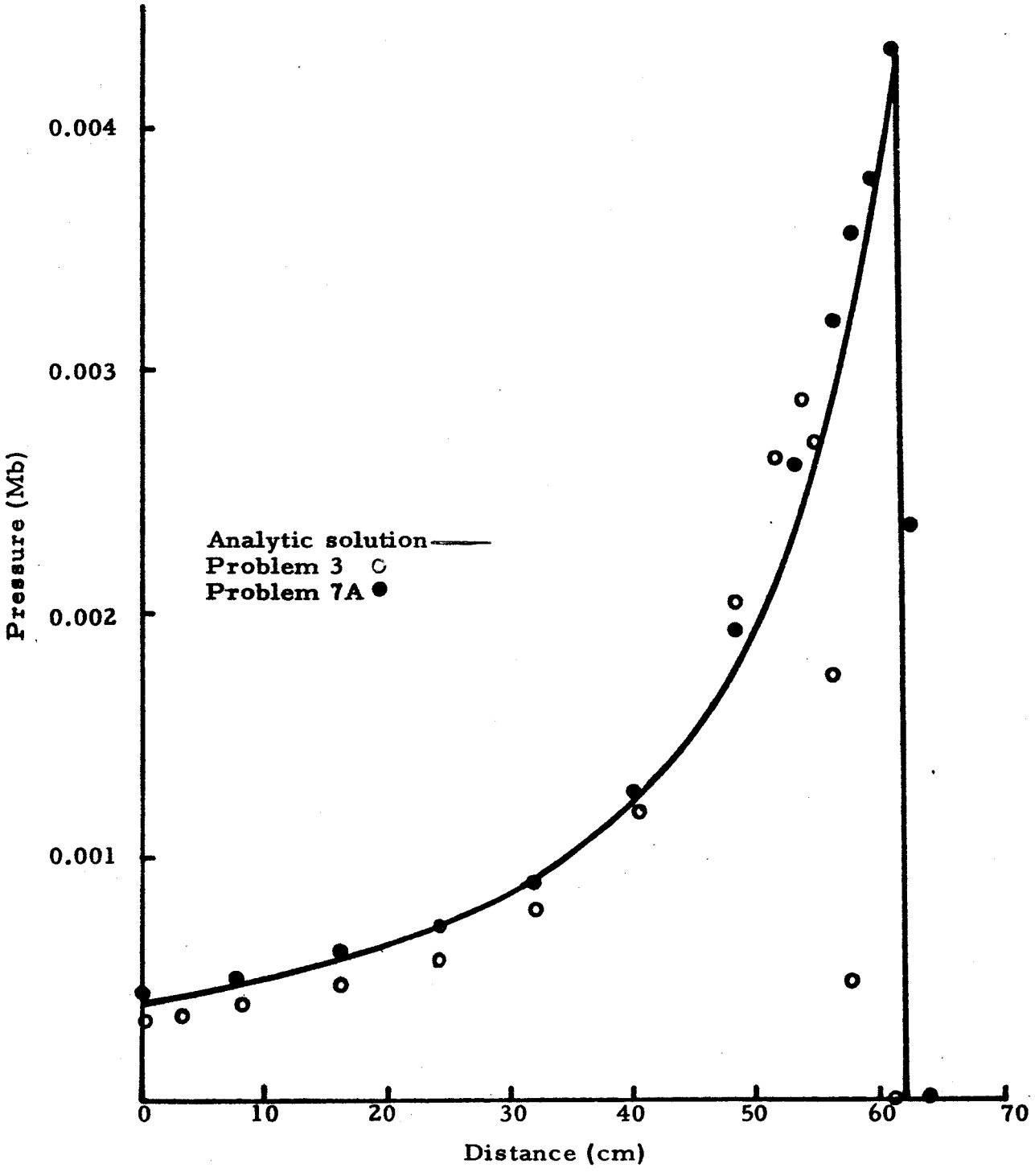

FIGURE 1. COMPARISON OF SOLUTIONS WITH OLD AND NEW EQUATIONS WITH THE ANALYTIC SOLUTION

B. DESCRIPTION OF GRANULAR MEDIA

1. Mohr-Coulomb Yield Model

The calculational program ELK, described in Section A, is designed to solve time-dependent problems of motion in a continuum. Each problem implicitly requires an equation of state for any medium involved. This equation must provide a relation between the state of stress, the state of strain, and the internal energy of the medium under any conditions that may be encountered. A problem may involve stresses varying continuously from tens of millions of atmospheres to tens of atmospheres, and it is extremely difficult to find a model to cover such a range.

For the region of stress between tens of megabars and 100 kb, the equation of state can be simplified to a relation between pressure, volume, and internal energy. In this region materials are generally hydrodynamic, and material strength properties are not important. In ELK this region would be calculated in an Eulerian coordinate system.

As stress levels are reduced below 100 kb, the nonisotropic nature of the stress tensor must be considered in the equation of state. It is in this lower pressure region that the crater begins to take its final form, and hence material strength properties become all-important.

For several reasons, a study of granite is a reasonable starting point toward an understanding of the dynamic response of geologic materials. First, the porosity of granite is negligible, so that there is no complication arising from irreversible compaction as in soils. Second, due to the lack or porosity, the initial density and other properties will be uniform from sample to sample, so that laboratory Hugoniot measurements may be applied with confidence to calculations of underground explosions. Third, there have been two underground nuclear tests in granite, SHOAL and HARD HAT, in which close-in measurements of ground shocks have been made. Both of these shots were deeply buried, with the result that the shock was spherically symmetric, and calculations to be compared with them may be done on a one-dimensional code.

Laboratory measurements on shock waves in granite (Ref. 5) indicate a precursor with an amplitude of 35 to 50 kb, much higher than typical elastic precursors in metals. There is probably a phase transition at this stress level, similar to that observed in quartz (Ref. 6). The precursor travels at a velocity nearly equal to the elastic sound speed. Shock-time-of-arrival measurements made by the Sandia Corporation on the HARD HAT event show a constant shock speed in the stress range of about 50 to 0.3 kb. The stress deviators are significant, for the shock velocity is larger than that calculated from the bulk modulus alone. All this evidence would suggest that the precursor is elastic. However, such a conclusion is contradicted by the measured attenuation of shock strength in the underground tests.

Consider the waveform in granite of the shock from an underground nuclear explosion in granite at a time at which the peak stress is 50 kb. The shock front will be steep, for any real viscosity will certainly be insignificant at this shock strength. Consequently, the compression will be small, so that the entropy increase from shock heating is negligible. From the theory of elastic wave motion, it is known that for a spherically symmetric wave with small amplitude and with a discontinuous rise at its front moving outward in an elastic medium, the stress at the wave front is inversely proportional to the radius. However, the peak stress measured in SHOAL and HARD HAT attenuates more rapidly, roughly proportional to R^{-2}. Therefore there must be some mechanism of energy absorption in granite that is effective at low stress levels. Our efforts have been directed toward investigating mechanisms that are not rate-dependent, and we have found one that successfully predicts the behavior of granite: Coulomb yielding. In this model the straight-line loading path for granite in one-dimensional compression is not interpreted as elastic, but rather as plastic with a yield stress that increases with pressure.

The Mohr-Coulomb yield condition is a generalization of Coulomb's proposal that internal friction in a solid may contribute to its yield stress. Consider a granular material with a coefficient of friction between the

grains of f and define an angle φ such that $\tan\varphi = f$. Let the maximum and minimum principal stresses be Σ_1 and Σ_3, and assume that they are compressive. As an example, consider a plane oriented 45 deg to the direction of Σ_1 and Σ_3. The shear stress on this plane is $1/2(\Sigma_1 - \Sigma_3)$, and the normal stress is $1/2(\Sigma_1 + \Sigma_3)$. Then the condition for slipping on this plane is

$$|\Sigma_1 - \Sigma_3| = \tan\varphi \; |\Sigma_1 + \Sigma_3|$$

When all other planes are considered, the necessary condition for slipping becomes

$$|\Sigma_1 - \Sigma_3| = \sin\varphi \; |\Sigma_1 + \Sigma_3| \tag{1}$$

The left side of this equation is the yield stress according to the Tresca condition, and it is also the yield stress in the von Mises formulation, based on the second invariant of the stress tensor, if one assumes that $\Sigma_2 = \Sigma_3$. This assumption will be used in the following work, since it is valid in spherical symmetry, which is the geometry in which the model will be tested. The right side of the above equation may be related to the pressure, and one obtains

$$Y = \frac{2\sin\varphi}{1 - 1/3\sin\varphi} P \tag{2}$$

where Y is the yield stress and P is the pressure. Define coefficients b and B by the equations $Y = bP$ and $\Sigma_1 = B\Sigma_3$. Relations between the coefficients are given from (1) and (2) as

$$b = 3\frac{B - 1}{B + 2} = \frac{2\sin\varphi}{1 - 1/3\sin\varphi}$$

$$B = \frac{1 + 2/3\,b}{1 - 1/3\,b} = \frac{1 + \sin\varphi}{1 - \sin\varphi}$$

Values of B that are good at low pressures are available for many rocks (Ref. 7).

At the compressive yield point ($|\Sigma_1| > |\Sigma_3|$),

$$-\Sigma_1 = (1 + 2/3\,b)\,P$$

and

$$-\Sigma_3 = (1 - 1/3\,b)\,P$$

Note that the coefficient b cannot be greater than 3, and that at positive pressures no stress can be tensile. In this model it is reasonable to require that the pressure be zero in expanded states, so that no tension is allowed.

The generalized Mohr-Coulomb yield condition states that the yield stress is an arbitrary function of pressure. The version currently employed in the codes is

$$Y = \text{minimum of } \begin{cases} a + bP \\ Y^o \end{cases}$$

where the upper limit, Y^o, may be interpreted as the von Mises yield point of the grains themselves (Figure 2). The coefficients a and b may be determined from the tensile strength T and compressive strength C of an unconfined specimen of rock by constructing a Mohr diagram. The results are:

$$a = 2\frac{CT}{C + T}$$

$$b = 3\frac{C - T}{C + T}$$

The stress a is typically less than 1 kb, even for competent (hard) rocks. Since we are primarily interested here in the stress range of tens of kilobars, much of the following discussion will be devoted to the simpler Coulomb model in which a = 0.

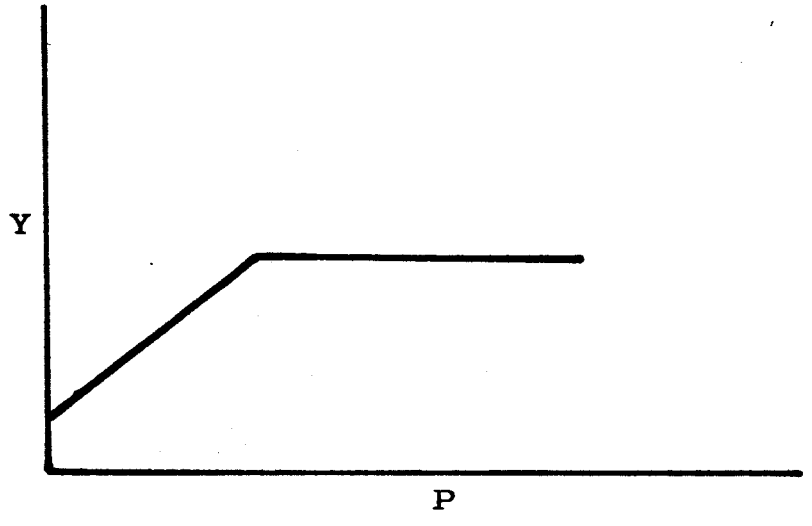

FIGURE 2. YIELD STRESS VERSUS PRESSURE FOR THE MOHR-COULOMB CONDITION

Depending on the relation between the coefficient of friction and Poisson's ratio, two different cases may be distinguished. If $(1 + \frac{2}{3}b)k > k + \frac{4}{3}\mu$, where k is the bulk modulus and μ is the shear modulus, then the yield stress increases so rapidly that yielding will not occur in one-dimensional plane compression. Note (Figure 3) that the quantity $(R + \frac{4}{3}\mu)$ is the slope in the plot of stress versus strain for the elastic case, while the quantity $\left[(1 + \frac{2}{3}b)\,k\right]$ is the slope in the plot of stress versus strain at the yield point. This condition is equivalent to

$$\nu > \frac{1}{B + 1}$$

where ν is Poisson's ratio. In the second case the inequality is reversed, and yielding will occur continually during loading in plane compression. In Figure 3 the pressure, stress in the direction of displacement, and limit on this stress determined by the yield condition are plotted against compression for the two cases. In spherical symmetry an additional variable, the radial displacement, enters, and yielding may occur in both cases, since a tensile hoop stress is not allowed. The second case has been found to give smoother solutions, and the particular models used so far have been of this type.

The effect of Coulomb yielding on an outward-moving spherical shock wave may be discussed qualitatively. Upon passage of the shock front, the stress deviators increase to values comparable to the pressure, which means that a substantial portion of the energy of loading, the "energy of distortion," goes into the anisotropic stress state. The material acquires a positive radial velocity, so that work is done against the stress deviators, while the radial displacement tends to prevent their relaxation. Yielding is taking place, thus this work is irrecoverable. The stress deviators are tending to slow down the motion of the material, but the total hoop stress, which cannot be tensile, will not contribute to any rebound. Furthermore, the pressure will eventually approach zero, reducing the yield stress and the stress deviators, so that the remaining energy of distortion is irrecoverable. Therefore the energy absorbed is

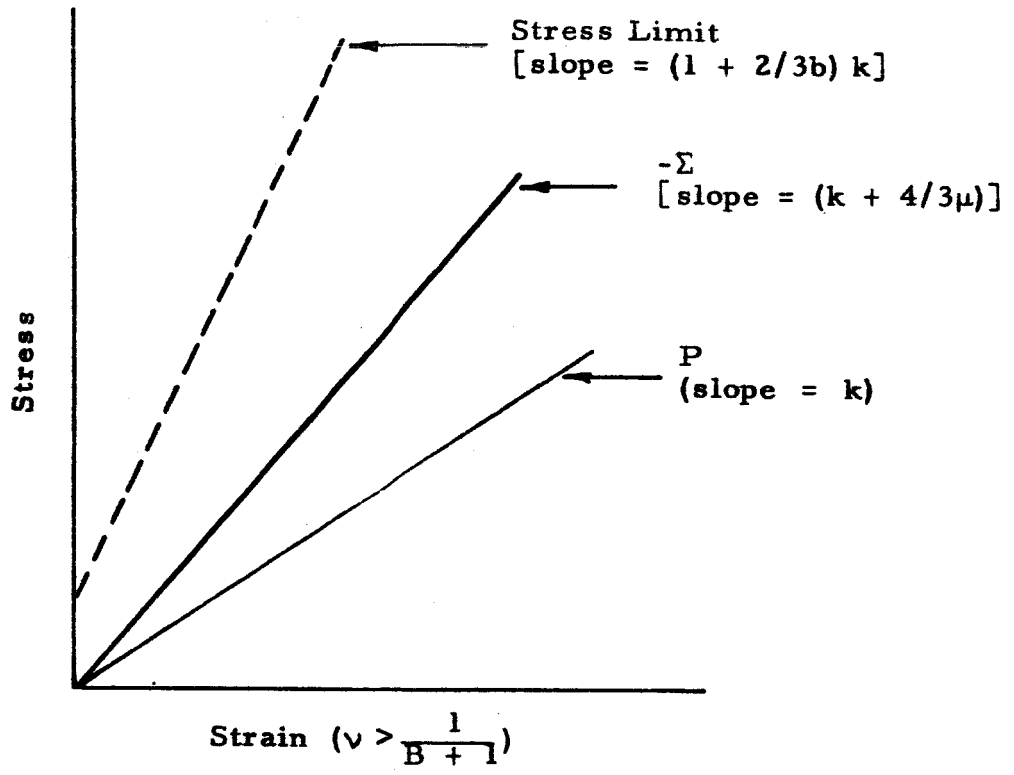

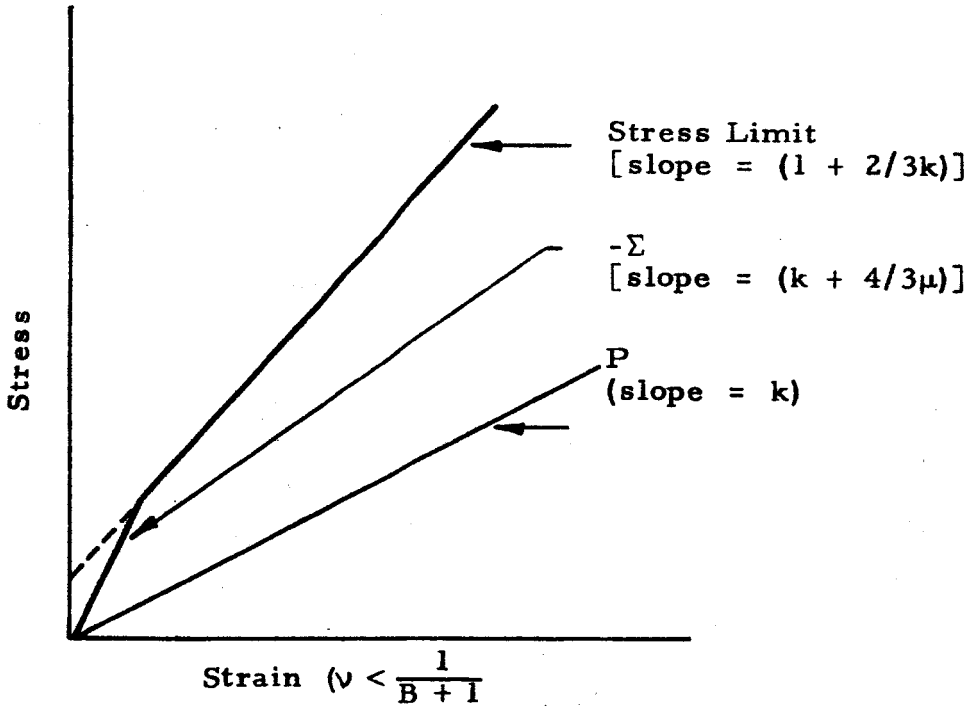

FIGURE 3. MOHR-COULOMB YIELD CONDITION. Pressure, normal stress, and the stress limit plotted against strain for one-dimensional plane compression

a significant fraction of the energy of loading throughout the stress range in which Coulomb yielding occurs.

By contrast, in the von Mises case at stress levels several times larger than the yield stress, the distortion energy is a small part of the total, and at stresses less than the yield stress the material is, of course, elastic. Therefore the energy lost to plastic work is important only in a limited stress range.

Also, it is worthwhile to compare the relaxation of a plastic wave after peak compression has been reached. In the case of a plane wave with either von Mises or Coulomb yielding, the expansion causes a relaxation of the stress deviators that is initially elastic. In the case of a spherical wave, the stresses are determined by the radial displacement as well as the compression. With von Mises yielding, the relaxation is elastic, but at a slower rate in the spherical than in the plane case. With Coulomb yielding, however, it has been observed in numerical code solutions for granite that there is no elastic relaxation near the shock. The reason is that the yield stress, being a function of pressure, depends on compression but not radial displacement and therefore decreases faster than the stress deviators would decrease elastically. The result is that the material is always yielding.

Time-dependent stress relaxation is one of the mechanisms that might account for the attenuation observed in granite. The effect of this mechanism might be similar to that of Coulomb yielding in regard to some of the points discussed above. The major difference is that Coulomb yielding is scalable, and consequently it will give the same attenuation for an energy source of any size.

The fact that there is no elastic relaxation behind a spherical shock in a medium with Coulomb yielding when reasonable parameters are used

may be utilized to find an analytic solution for the attenuation. It is assumed that

$$Y = bP \quad \text{and}$$

$$(1 + \frac{2}{3}b)k < k + \frac{4}{3}\mu$$

so that the material is yielding everywhere, and is at the compressive yield point. Then there is the unique relation between the principal stresses,

$$\Sigma_r = B\Sigma_\theta$$

where Σ_r is the radial stress and Σ_θ is the tangential stress. This unique relation makes a solution feasible. The only additional assumption is that the compression is small.

The system of equation to be solved is:

Equation of Motion

$$\rho_o \frac{1}{V} \frac{\partial u}{\partial t} = \frac{\partial \Sigma_r}{\partial r} + 2\frac{\Sigma_r - \Sigma_\theta}{r} \tag{3}$$

Equation of Continuity

$$\frac{\dot{V}}{V} = \frac{\partial}{\partial t}(\ell n V) = \frac{1}{r^2}\frac{\partial (r^2 u)}{\partial r} \tag{4}$$

Equation of State (small-amplitude approximation)

$$-\frac{1}{3}(\Sigma_r + 2\Sigma_\theta) = P = +k(1 - V) \tag{5}$$

Yield Condition

$$\Sigma_r = B\Sigma_\theta \tag{6}$$

where u is the radial velocity and V is the relative volume.

In the small-amplitude approximation, the factor 1/V in the equation of motion may be assumed as unity. Using the yield condition one finds

$$P = -\frac{B+2}{3B}\Sigma_r$$

$$\Sigma_r - \Sigma_\theta = \frac{B-1}{B}\Sigma_r$$

so that P and Σ_θ may be eliminated from the system of equations. The equation of state becomes

$$\Sigma_r = -\frac{3B}{B+2}k(1-V)$$

Therefore

$$c \equiv \frac{1}{\rho_o}\frac{\partial}{\partial V}\Sigma_r = \sqrt{(\frac{3B}{B+2}k)/\rho_o}$$

The system of equations (3 through (6) reduces to

$$\rho_o\frac{\partial u}{\partial t} = \frac{\partial \Sigma_r}{\partial r} + \alpha\frac{\Sigma_r}{r} \tag{7}$$

$$\frac{1}{\rho_o c^2}\frac{\partial \Sigma_r}{\partial t} = \frac{\partial u}{\partial r} + 2\frac{u}{r} \tag{8}$$

where $\alpha = 2(B - 1/B)$. Equations (7) and (8) are to be solved for an outward-moving shock. At the shock front $r = ct$ and $\Sigma_r = -\rho_o cu$. As shown below,

the shock strength may be found as a function of distance without obtaining a complete solution. Qualitatively, the reason is that the sound speed in this case is constant, so that no signal can overtake the front. A series of substitutions of variables will make the problem more amenable.

Let $$\Psi = \Sigma_r + \rho_o cu$$

$$\Phi = \Sigma_r + \rho_o cu$$

Then equations (7) and (8) become

$$\frac{1}{c}\frac{\partial \Psi}{\partial t} = \frac{\partial \Psi}{\partial r} + \left(1 + \frac{\alpha}{2}\right)\frac{\Psi}{r} - \left(1 - \frac{\alpha}{2}\right)\frac{\Phi}{r}$$

$$\frac{1}{c}\frac{\partial \Phi}{\partial t} = -\frac{\partial \Phi}{\partial r} + \left(1 - \frac{\alpha}{2}\right)\frac{\Psi}{r} - \left(1 + \frac{\alpha}{2}\right)\frac{\Phi}{r}$$

Let $$\psi = r^{(1+\alpha/2)}\Psi$$

$$\varphi = r^{(1+\alpha/2)}\Phi$$

then $$\frac{1}{c}\frac{\partial \psi}{\partial r} = \frac{\partial \psi}{\partial r} - \left(1 - \frac{\alpha}{2}\right)\frac{\varphi}{r}$$

$$\frac{1}{c}\frac{\partial \varphi}{\partial t} = -\frac{\partial \varphi}{\partial r} + \left(1 - \frac{\alpha}{2}\right)\frac{\psi}{r}$$

Let $$\xi = r - ct$$

$$\zeta = r + ct$$

Then the system of equations becomes

$$\frac{\partial \psi}{\partial \xi} = \left(1 - \frac{\alpha}{2}\right)\frac{\varphi}{\xi + \zeta}$$

$$\frac{\partial \varphi}{\partial \zeta} = \left(1 - \frac{\alpha}{2}\right)\frac{\psi}{\xi + \zeta}$$

The boundary condition

$$\Sigma_r = -\rho_o cu \quad \text{at} \quad r = ct$$

is equivalent to

$$\psi = 0 \quad \text{at} \quad \xi = 0$$

Therefore, at the shock front

$$\frac{\partial \varphi}{\partial \zeta} = 0$$

$$\varphi = C$$

$$\Sigma_r = -\rho_o cu \frac{1/2\, C}{r^{(1+\alpha/2)}} = \frac{1/2\, C}{r^{(2-1/B)}}$$

where C is a constant of integration. If a material has no internal friction, then B is equal to 1, and the shock strength is inversely proportional to the first power of the radius, as it should be for the case of a spherical wave of small amplitude in a lossless medium. For larger coefficients of friction the attenuation is larger, up to a limit of an inverse square dependence for an infinite coefficient of friction. This last case is equivalent to the requirement that Σ_θ be zero. In some calculations reported by other workers (Ref. 8), the hoop stress is not allowed to be tensile. It may be seen that at points in space-time where it is effective, such a requirement is equivalent to Coulomb yielding. The attenuation obtained in such calculations is related to the above analysis.

2. Diatomaceous Earth Experiment and One-Dimensional Calculation

In order to understand the phenomenon that occurs when a shock interacts with a porous material, an experiment was undertaken to observe the formation of a crater in diatomaceous earth caused by a nylon pellet

traveling at approximately 22,000 ft/sec. A computer calculation using a polynomial type of equation-of-state model was done concurrently.

Radiographic exposure tests showed that a nylon projectile of 0.250-in. outside diameter could be sufficiently resolved in diatomaceous earth whose X-ray absorption path was three times the diameter of the projectile. The density of the earth was 0.33 g/cm^3 and was contained at one atmosphere by a tubular cylinder of polyester film having an outer diameter of 0.750 in. and a wall thickness of 0.002 in. The bore diameter of the barrel used to accelerate the projectile was 0.252 in. and was fitted with an 0.137-g nylon projectile whose length-to-diameter ratio was 0.5. The experimental results of this shot are shown in Figures 4, 5, and 6.

Figure 4 is a radiograph of the crater formed in the diatomaceous earth 8.4 μsec after impact. The highly compressed (snow-plowed) earth gives a "new moon" effect to the front edge of the crater. It is interesting to note the relatively high-density tubular corridor leading to the front edge of the crater. This corridor is believed to be formed by the ablated edges of the nylon projectile; tunneling of the projectile through the low-density diatomaceous earth has caused erosion of the projectile. To the author's knowledge, this phenomenon has not been dynamically observed before. At the time of the radiograph (8.4 μsec after impact) there were no perceptible ejecta from the crater. The color framing-camera sequence did not show ejecta by this time either. Figure 5, a, b, c, and d are excerpts from the framing-camera sequence showing the flight of the projectile as it emerged from the muzzle of the gun (5a), struck an 0.002-in. polyester film X-ray switch (5b), continued downrange (5c), and entered the diatomaceous earth target (5d). The optical view is perpendicular to the radiographic view of Figure 4. The motion of the projectile as determined from the optical and radiographic records is given in Figure 6. This figure shows that the projectile had an average velocity of 0.226 cm/μsec during its deceleration from the moment of impact to 8.4 μsec after impact.

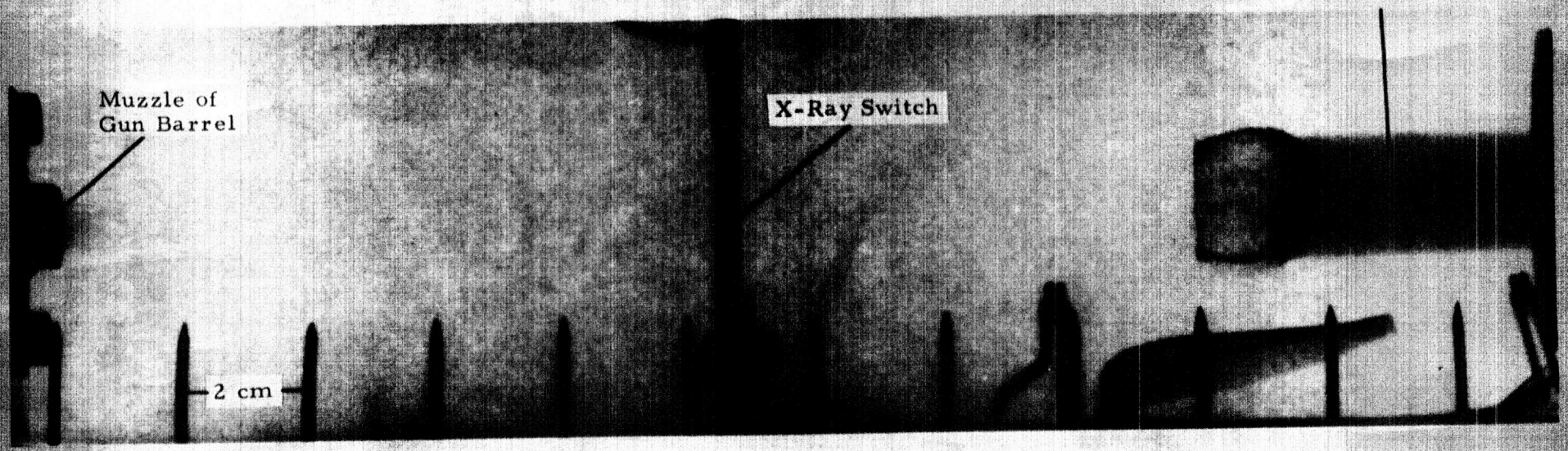

FIGURE 4. DYNAMIC RADIOGRAPH OF CRATER FORMING IN DIATOMACEOUS EARTH AFTER THE IMPACT OF NYLON PROJECTILE WITH A VELOCITY OF 22,000 ft/sec (Shot CLG-13)

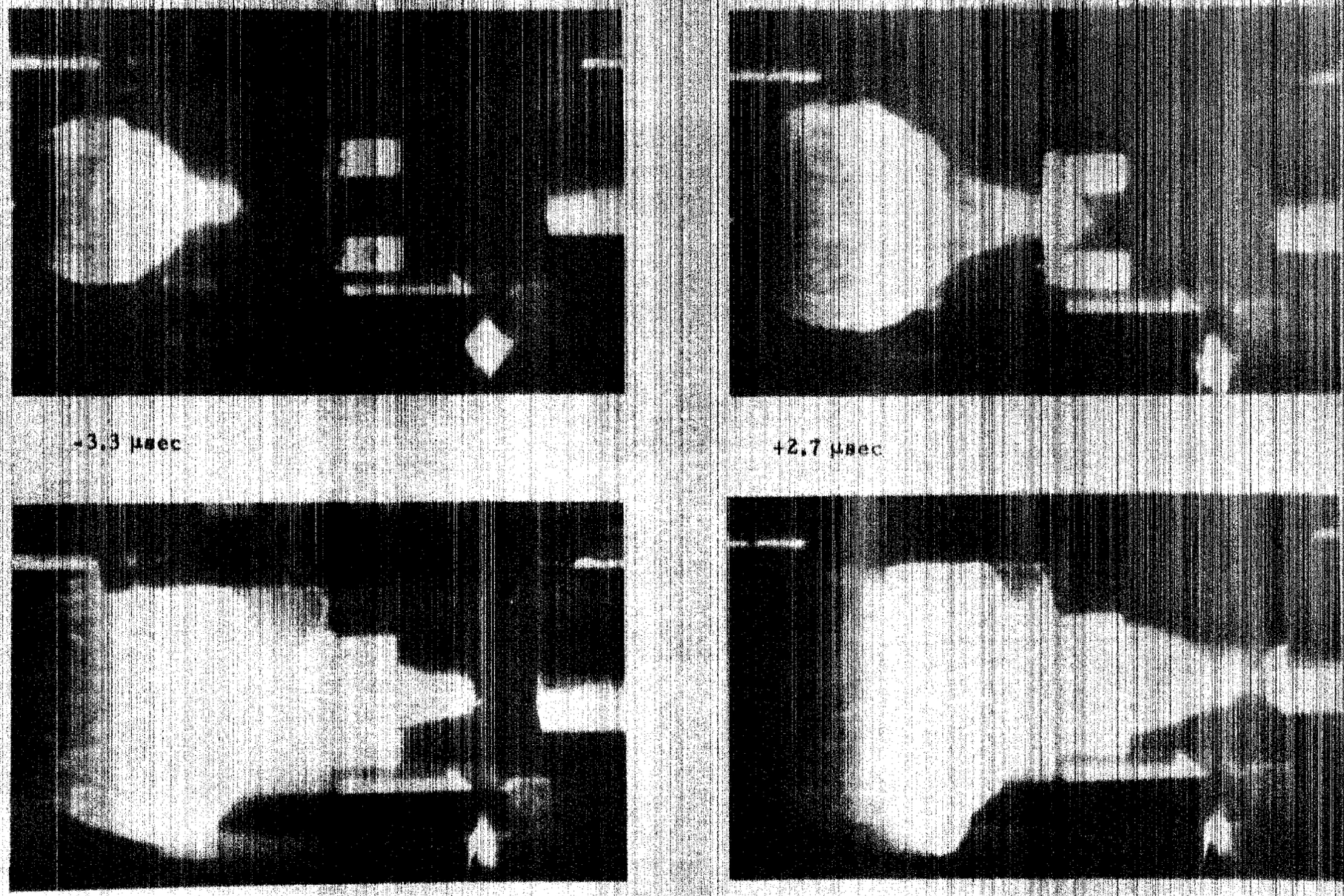

FIGURE 5. FRAMING-CAMERA SEQUENCE OF SHOT CLG-13 SHOWING PROJECTILE MOTION AND IMPACT OF DIATOMACEOUS EARTH TARGET

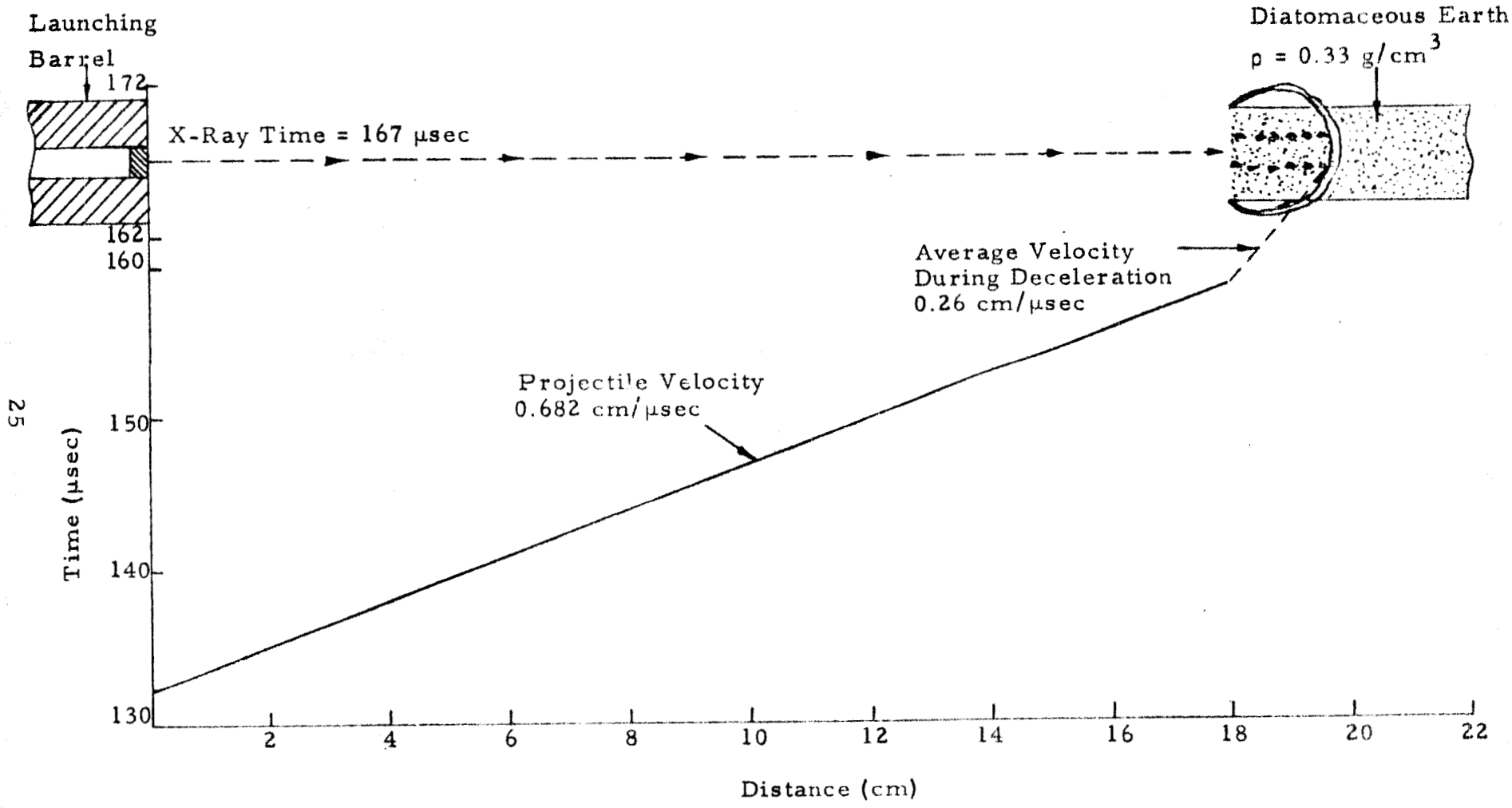

FIGURE 6. EXPERIMENTALLY DETERMINED POSITION-TIME HISTORY OF SHOT CLG-13

The impact of this shot was simulated by a one-dimensional computer calculation. The calculation began at impact and continued to 10 μsec after impact. Since the equation of state and material properties of the low-density diatomaceous earth is not known, the equation of state and material properties of quartz were used because of their similar siliceous properties. The initial density of the quartz (2.66 g/cm^3) was expanded to that of the diatomaceous earth (0.33 g/cm^3). The results of this calculation are given in Figure 7. The depth of penetration after 8.4 μsec is shown to be 2.45 cm, compared to the experimentally determined 2.0 cm. The agreement of the experiment and computation is rather good considering that no two-dimensional effects, such as the mushrooming of the projectile and lateral rarefactions, have been included.

3. Particle Impact Problem

In order to understand the processes or mechanisms present when a shock compresses a porous material, a computer run was proposed to investigate the compaction process on a microscopic level. This work obtained some impetus as a result of the conclusions presented in Reference 8. The paper presented the view that particle interactions resulted in an equilibrium state situated on the Hugoniot of the compact solid.

Specifically, a run was made to simulate some Stanford Research Institute Hugoniot data for 1.55 g/cm^3 playa (Ref. 10) by considering quartz "particles" in a state of 41 per cent porosity. The problem was done on REDOC (Physics International's one-dimensional, elastic-plastic, Lagrange code) with a void closure option added. The geometry used was that of plane symmetry and is shown in Figure 8. The quartz "particles" (infinite plates of finite thickness in one-dimensional plane symmetry) were arranged in such a way that the width of the void between them was 41 per cent of the distance from one "particle" to the next.

A shock was initiated on the left side of the aluminum driver plate with a constant-velocity piston (to simulate a flyer plate) consistent with

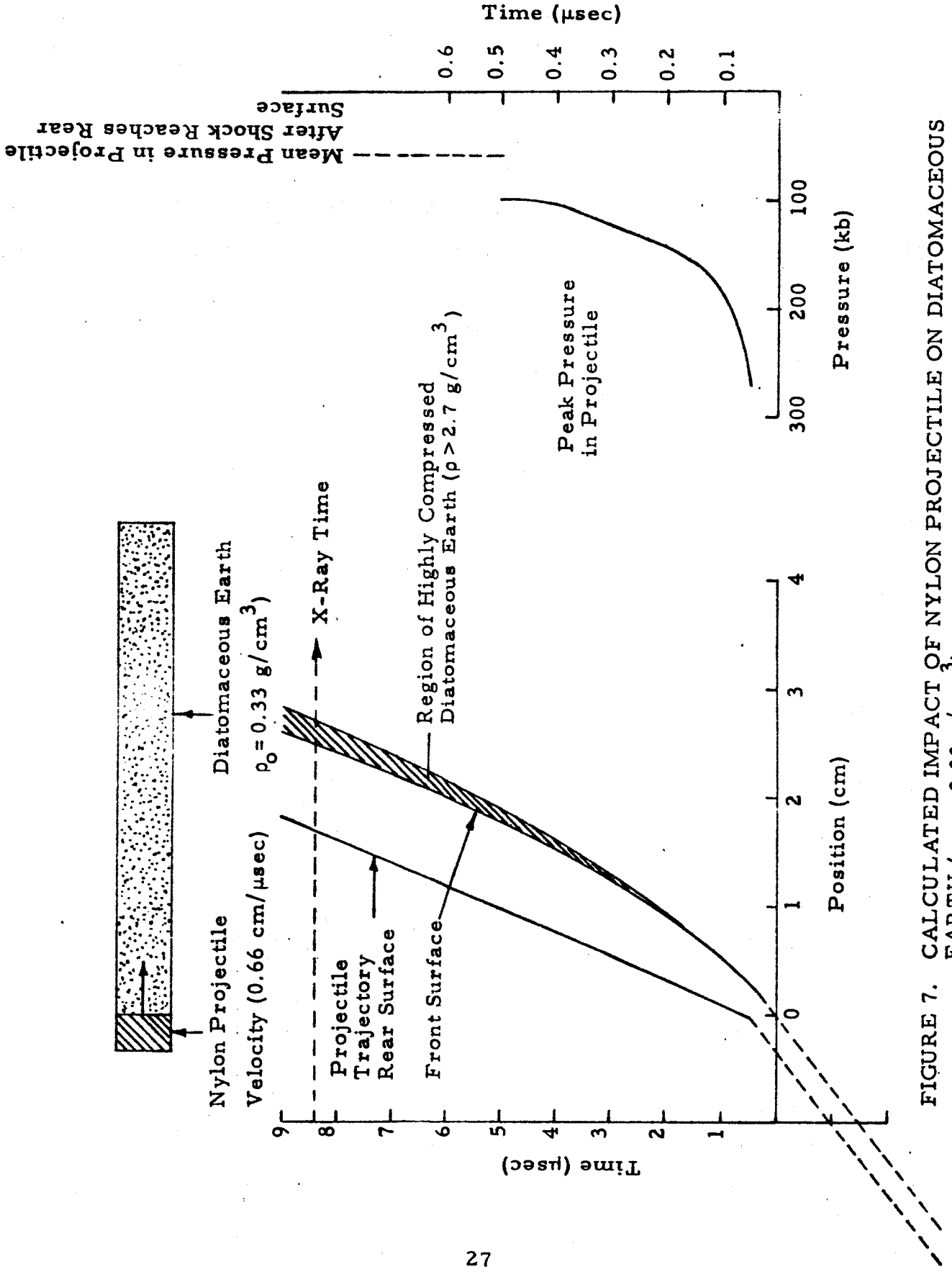

FIGURE 7. CALCULATED IMPACT OF NYLON PROJECTILE ON DIATOMACEOUS EARTH (ρ_o = 0.33 g/cm^3)

1445

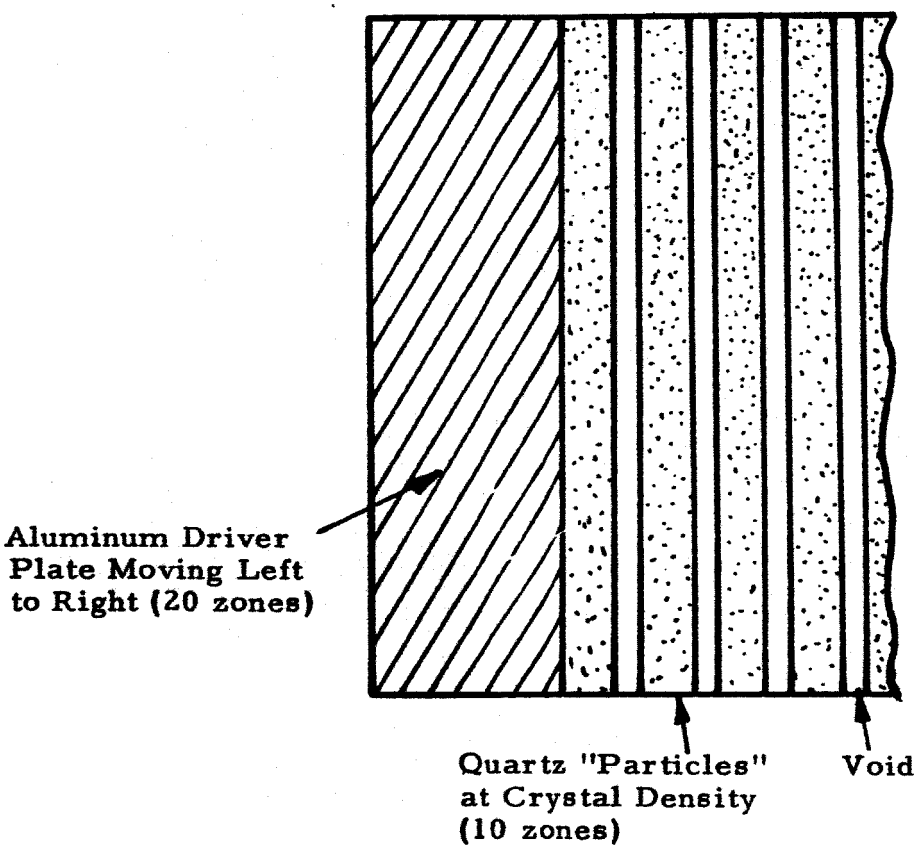

FIGURE 8. CALCULATIONAL MODEL FOR POROUS PLAYA

2036

the driver plate pressure shown for Shot No. 10,605 in Table I of Reference 10. The shock proceeded through the driver plate and into the quartz "particles." As the voids were closed, the shock was transmitted from one particle to another. It was hoped that after the shock had traveled through several particles in our calculations, pressure and relative volume would begin to settle to some equilibrium state consistent with the experimental findings in the Stanford report.

After the shock had traveled through eight particles the results could not be said to be conclusive. The interactions among the particles were too violent for an equilibrium condition to exist at this early time. However, average particle velocity was within 50 per cent of that measured, and the average shock speed was about 15 per cent higher than the measured shock speed.

A second identical problem was attempted with a viscous damping term that was a linear function of the rate of change of relative volume. Its purpose was not to simulate any real viscosity, but rather to eliminate any calculational noise that might be contributing to the nonequilibrium state. Again nothing conclusive was noted. The results of this run showed an average particle velocity almost equivalent to that measured, but the shock velocity dipped to a value 15 per cent below the observed value.

These two problems indicate that the microscopic approach toward a more complete understanding of the compaction process may be worthwhile. Neither run is conclusive in its present state. For example, the first problem could be run considerably farther to allow more time for an equilibrium configuration to develop. The second problem, on the other hand, indicated that some work with respect to the effects of different viscosity models would be profitable. It is apparent that some form of damping occurs during the compaction process; the problem is to mock it up in a realistic manner.

Furthermore, the void closure option in REDOC could be expanded to allow for internal spalling at particle boundaries. There are very few spall data available, but it may be important to include this mechanism in the model. Finally, if the one-dimensional approach is fruitful, then a problem considering two-dimensional effects could be done on PIPE (Ref. 3).

4. Equation-of-State Library

A capability is being developed to efficiently gather and correlate the ever-increasing amount of experimental data for granular substances. It is felt that an up-to-date library of equations of state and material properties is essential to the calculation and analysis of cratering phenomena.

At the present time a least-squares code has been developed to derive an equation of state of the form

$$P = a_o + a_1\mu + a_2\mu^2 + a_3\mu^3, \quad \text{where} \quad \mu = \frac{\rho}{\rho_{ref}} - 1$$

to fit Hugoniot data of different initial densities with respect to some arbitrary reference density. A plot is created simultaneously showing what the fit looks like with respect to the data points. An example of this capability is shown in Figure 9.

A literature search is also providing a catalogue of material information ranging from experimental data to theoretical papers. The data are evaluated as described above, and the theoretical works are considered in terms of their applicability to new models in the code.

This facility is in its developing phase, but it already promises to be a valuable tool. A code that will correlate data with respect to reliability is being worked on. The limits within which this code will work are not yet well defined. Its primary object will be to give confidence in combining Hugoniot data from different types of experiments. However, it is foreseen that a criterion for finding solid-to-solid phase transitions solely from Hugoniot measurements might also be achieved.

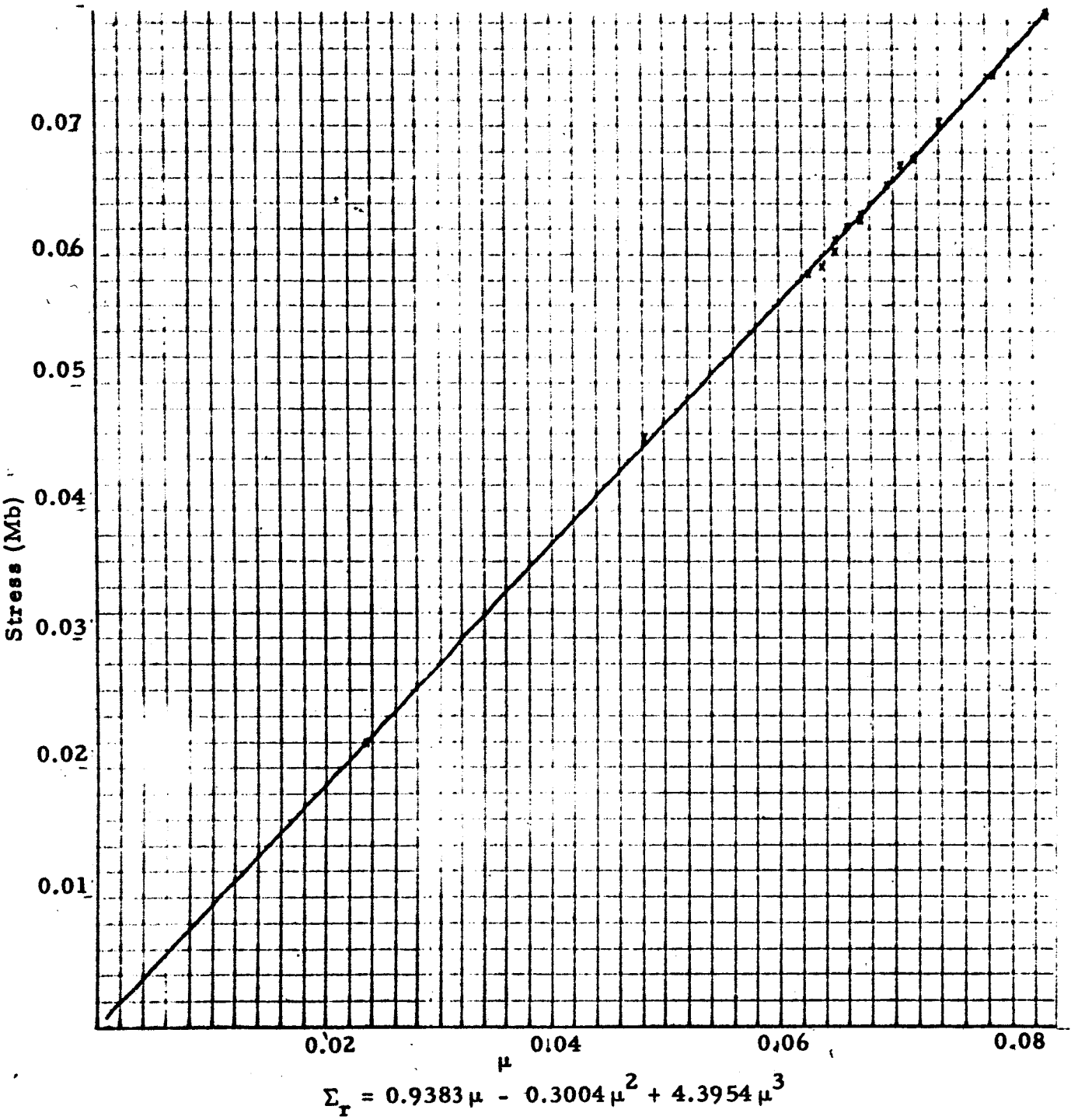

FIGURE 9. EXAMPLE OF LEAST SQUARES CAPABILITY

SECTION III

CRATERING PROBLEMS

A. DANNY BOY CALCULATION

1. Background

The DANNY BOY nuclear event was a 0.42-kiloton cratering experiment in volcanic basalt. The charge was placed 33.5 m (~110 ft) below the surface of Buckboard Mesa, Nevada. The geology at the site consisted of layers of both dense and vesicular basalt below which were beds of alluvium and tuffaceous rock. The charge was located in a horizontal band of dense basalt approximately 43 m (140 ft) thick. See Figure 10 (Ref. 11).

2. Problem Set-Up

The geological configuration of the calculation is shown in Figure 11. Layers less than 5 m (~15 ft) thick have been ignored or combined with other small layers. It was necessary to approximate the stratification shown in Figure 10 in order to optimize the zoning of the problem.

Homogeniety of the dense basalt to a radius of at least 27 m (90 ft) from the charge allowed the calculation in this region to be carried out on REDOC. This code, a one-dimensional analog to the PIPE code (Ref. 3), was appropriate for the spherical geometry of the initial expansion. The advantage of using REDOC in this region comes from the fine zoning possible at early times for excellent definition of the shock front. As the stress wave moves away from its source, its characteristic width enlarges and the width of the zones describing the wave may be enlarged. Also, less spatial definition is required in regions over which the shock has passed. Since zone size controls the time step of the problem (which affects the computer time), it is not advisable to use more zones than are necessary. Built into REDOC is a rezone scheme that satisfies all the above requirements in a

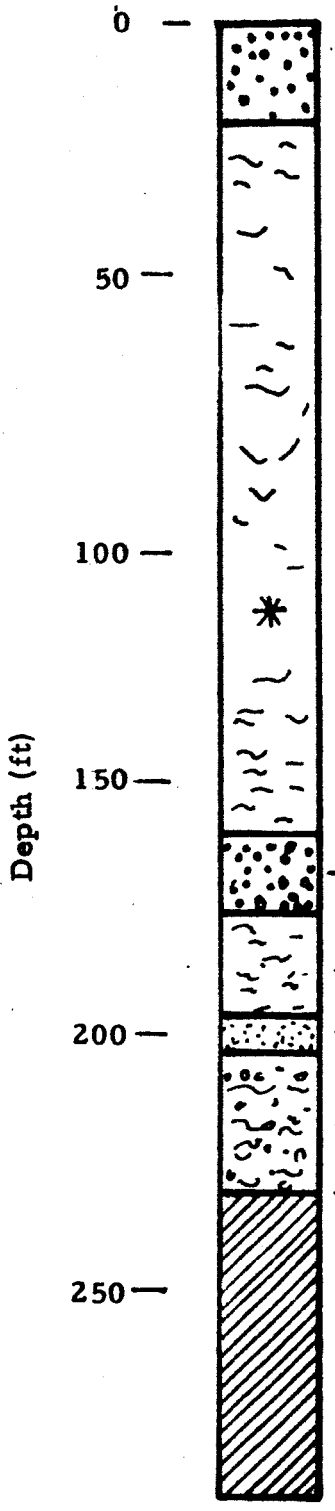

Depth	Description	Average Density
0-19.5 ft	Brown to gray vesicular basalt, few cinders, 10-40 per cent visicular	2.25 g/cm^3
19.5-160 ft	Gray, dense, nonvesicular basalt	2.62 g/cm^3
Shot Point		
160-175 ft	Reddish-brown vesicular basalt	2.17 g/cm^3
175-196 ft	Gray, dense, nonvesicular	2.62 g/cm^3
196-201 ft	Gray to brown basalt, some cinders	2.17 g/cm^3
201-229 ft	Gray vesicular to nonvesicular basalt, 15-40 per cent vesicular	2.24 g/cm^3
Alluvium and tuffaceous rocks		

FIGURE 10. COLUMNAR SECTION SHOWING SEQUENCE OF BASALT UNITS AS DETERMINED FROM CORE DATA, 25 ft south of DANNY BOY Surface Zero

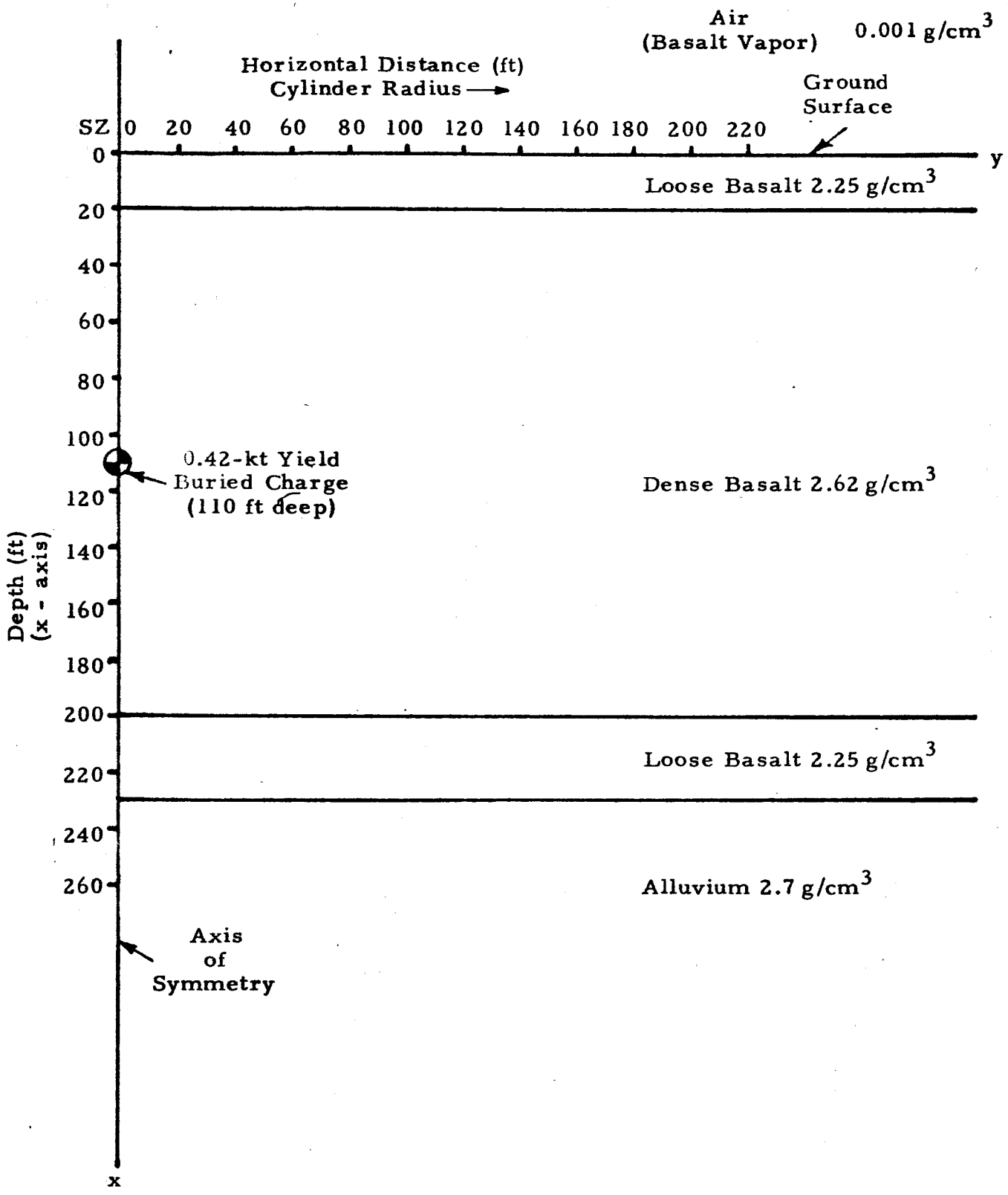

FIGURE 11. CHARGE LOCATION WITH RESPECT TO GEOLOGY IN DANNY BOY

very efficient way. When an automatic rezone is called for, the code doubles the spatial length of the problem while holding the number of zones constant. The sizes of the zones are made approximately twice their original sizes. The range of the one-dimensional REDOC solution is shown in Figure 12. Three rezones were used to get the activity to this radius. A grid 350 cm in radius with zones 8-1/3 cm wide began the problem. This grid was rezoned to 700 cm and approximately 16-2/3 cm zones, then to 1400 cm and approximately 33-1/3 cm zones, and finally to 2800 cm (90 ft) and approximately 66-2/3 cm zones. The nuclear source in the first grid was mocked up by introducing 1.76×10^{19} ergs of internal energy into a spherical mass of basalt 50 cm in radius. Since the initial zones were 8-1/3 cm wide, six zones described the charge. This source configuration was consistent with experience gained in computing similar problems. An indication of the effectiveness of the automatic rezoner is shown in Figure 13. In this plot of peak material velocity versus distance the effect of the first rezone is indicated by the letter A, the second rezone by the letter B, and the third rezone by the letter C. The smoothness of transition shows that no important detail was smeared out in the rezone process.

Once the activity passes through a change-of-density interface, the problem is no longer spherically symmetric and REDOC is no longer applicable. At this point the two-dimensional ELK code must be introduced. The activity profile in the REDOC solution was mapped onto the ELK grid shown in Figure 14. The Eulerian portion of the grid was created in such a way as to contain all material that might be appreciably displaced during the formation of the crater. The Lagrangian grid overlays the Euler grid in the region where strength considerations are important, and extends beyond it into regions that would experience relatively low peak stresses. The ELK grid has a typical zone size of 300 cm (~10 ft) up to a radius of 200 ft from the source. Beyond this point the size of each zone increases by 10 per cent as the radial distance from the source increases. Because ELK has no automatic procedure to implement the necessary mapping, the

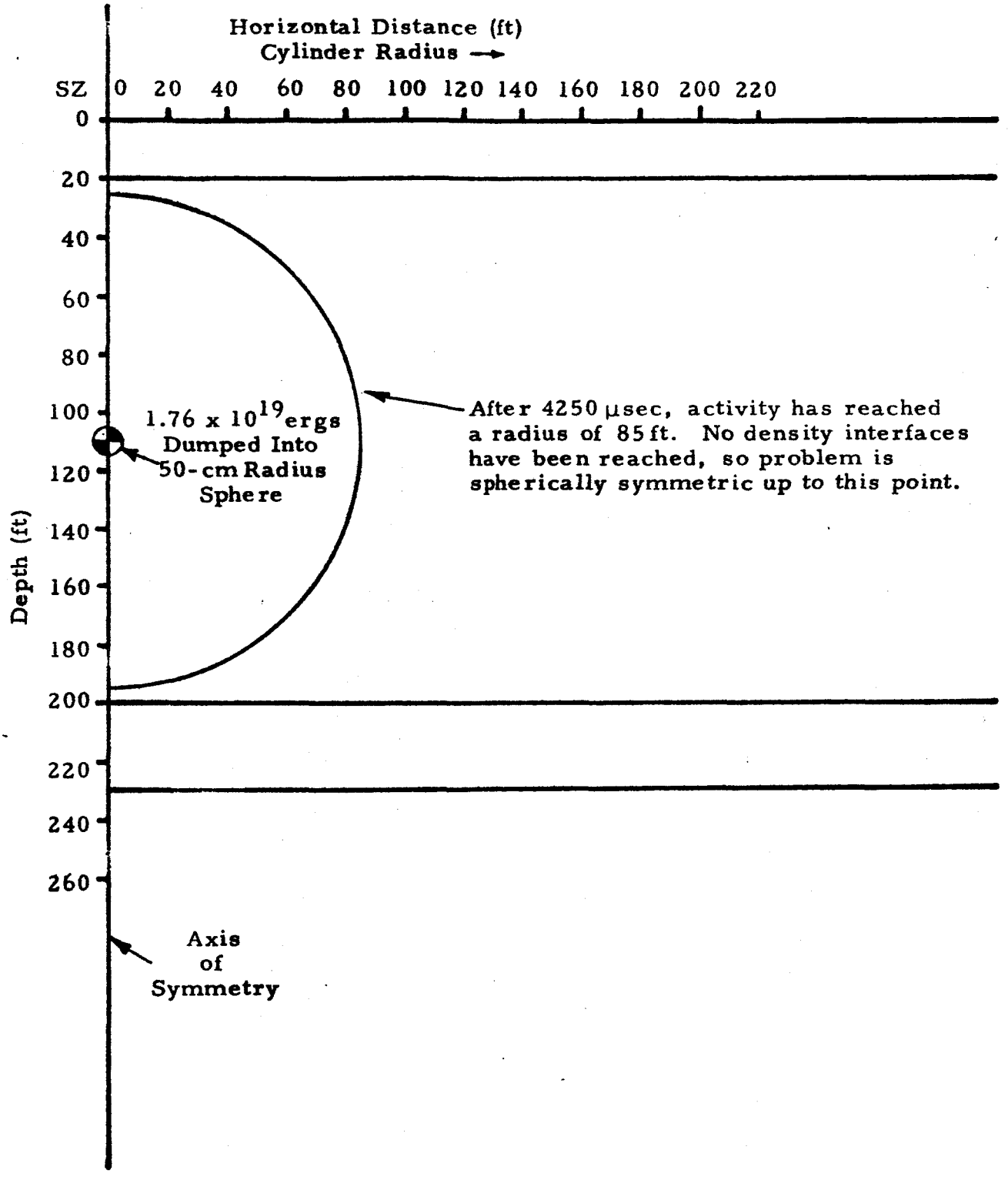

FIGURE 12. EXTENT OF ONE-DIMENSIONAL, SPHERICALLY SYMMETRIC CALCULATION IN DANNY BOY

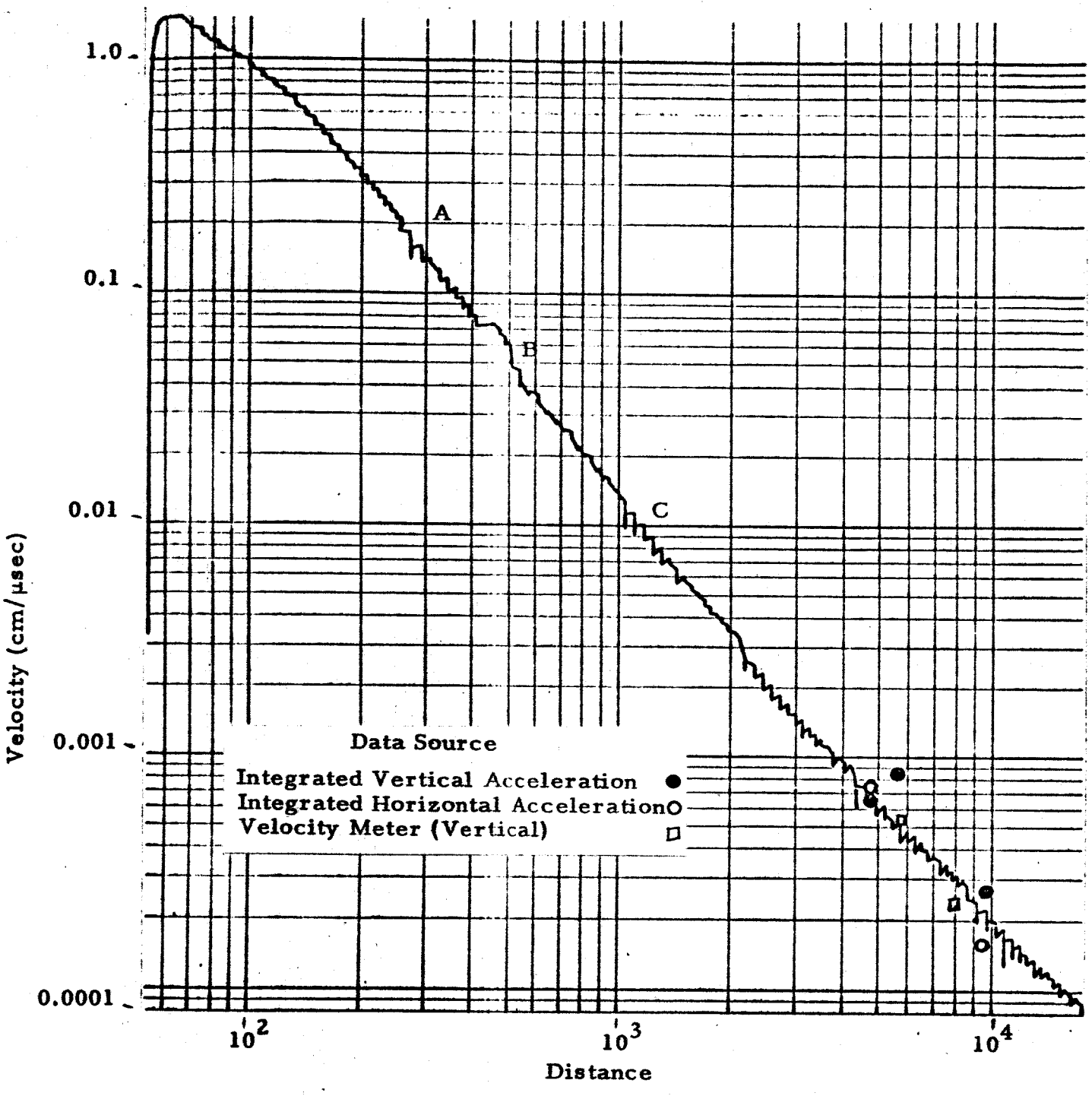

FIGURE 13. PEAK MATERIAL VELOCITY ATTENUATION IN DENSE BASALT

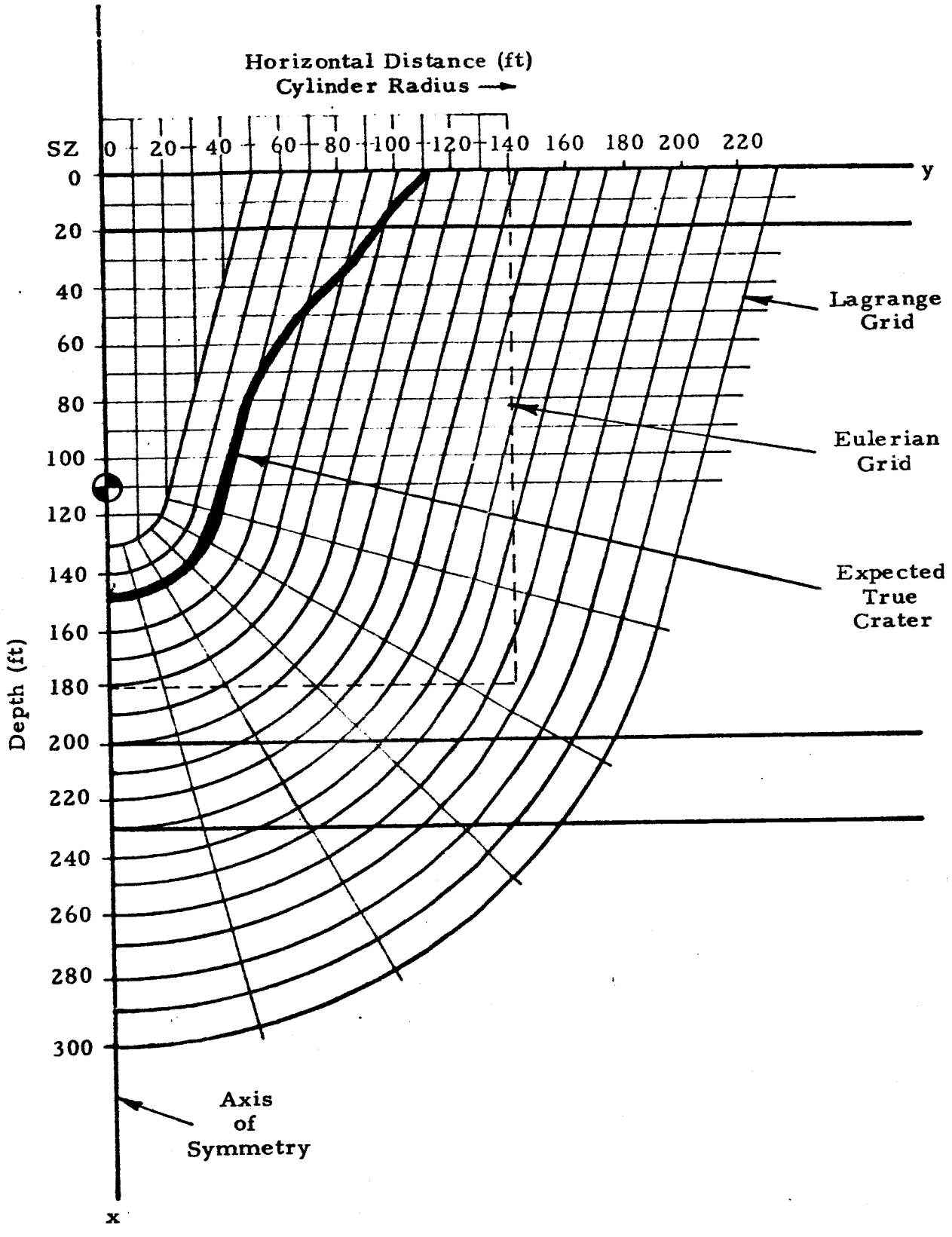

FIGURE 14. ELK GRID FOR DANNY BOY

1906

REDOC information was mapped manually onto the ELK grid. Care was taken to preserve all the important details calculated by REDOC.

A polynomial-type equation of state of the form $P = f(E, V)$ was used to describe the dense basalt throughout the entire problem. This was possible because after the first 100 μsec peak stresses were well below the 1-Mb restriction placed on this type of equation of state. Compressional sound speed in the basalt was given to be about 15,000 fps in Reference 12. Using the assumption that the compressional sound speed is $\sqrt{3}$ times greater than the shear sound speed, a material shear modulus of 0.1826 and a material bulk modulus of 0.3036 were calculated. These results used in equations of state for low-pressure description were obtained from equations (5a) and (7a), respectively, in Appendix A. Peak particle velocity data from the DANNY BOY event reported in Reference 12 were used to determine the energy-dependent coefficients in the equation of state. The final form of the equation of state for the dense basalt was

$$P = 0.3036\mu + 0.4\frac{E}{V}, \quad \mu = \frac{1}{V} - 1.$$

The peak particle velocity plot of Figure 13 came about as a result of the application of this equation of state in REDOC. The agreement with the DANNY BOY data points plotted is excellent.

For the layers of loose basalt in the Lagrange grid of ELK, a compaction equation of state described in Reference 1 was used. The model employs a hysteresis loop composed of a loading curve, whose derivation is shown in Appendix B, and unloading paths derived from the dense basalt given by $dP/d_\mu = 0.3036$. In the Euler grid the loose basalt used the equation of state of the dense basalt but had an initial density consistent with the loose basalt.

The yield model used was the Mohr-Coulomb model described earlier. Very little basalt data was available. The coefficients used resulted in the equations:

Von Mises yield stress = 0.0349

Coulomb yield stress = 0.0004 + 1.308 P.

Furthermore, the basalt was specified to have no resistance to tensile forces. These conditions lead to the Mohr envelope shown in Figure 15.

3. Results

Prior to the ELK computation, a hand calculation was made to see how much energy was necessary to lift the basalt rock out of the expected "true" crater. The necessary energy was found to be less than 1 per cent of the initial source energy. Thus it was felt that the effect of gravity would be trivial at least at early times and could be ignored. (At late times the formation of the "apparent" crater would be affected.)

Figure 16 shows the formation of the DANNY BOY crater at a time when the ground shock has traveled about 400 ft from the source. A velocity field has been superimposed on the original grid configuration. It should be noted that in actuality the Lagrange grid has been somewhat distorted at this time. Pressures where they exist are too small to affect any further cratering action. Velocities to the left of the expected true crater are such that particles would move approximately 5 to 10 feet against a gravity field. If gravity were imposed at this stage the particles would be expected to fall back and fill up the true crater, forming the apparent crater. The results of the DANNY BOY calculation clearly show that a crater has been formed in the vicinity of the expected crater. Finer zoning in the ELK stage of the calculation would no doubt have resulted in clearer definition of the crater. However, any significant reduction of zone size would have increased computer time greatly. If finer zoning were to be used in a subsequent calculation, an equation of state with a more realistic gas bubble description should be used. An example of a better description might be the so-called "Tillotson equations of state."

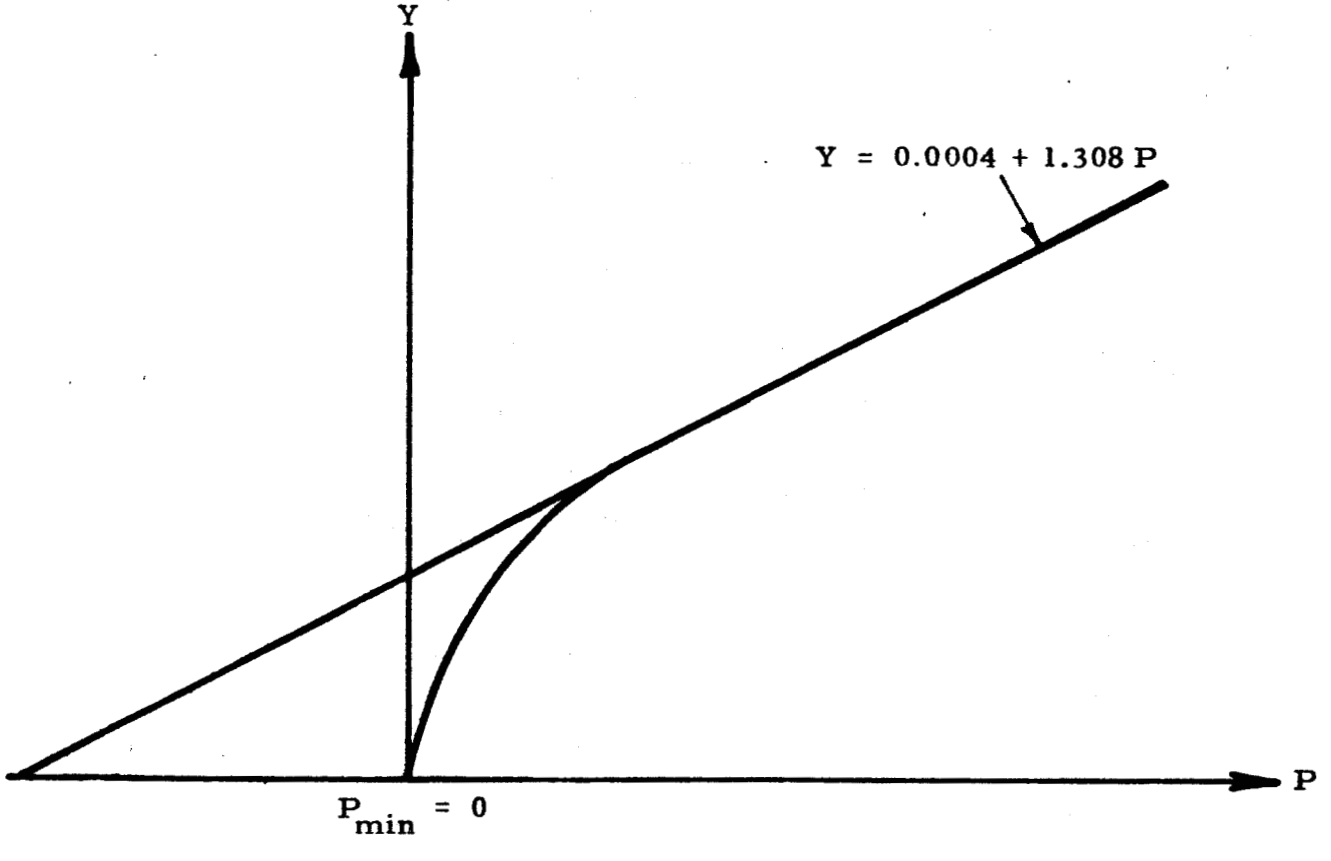

FIGURE 15. MOHR ENVELOPE FOR BASALT

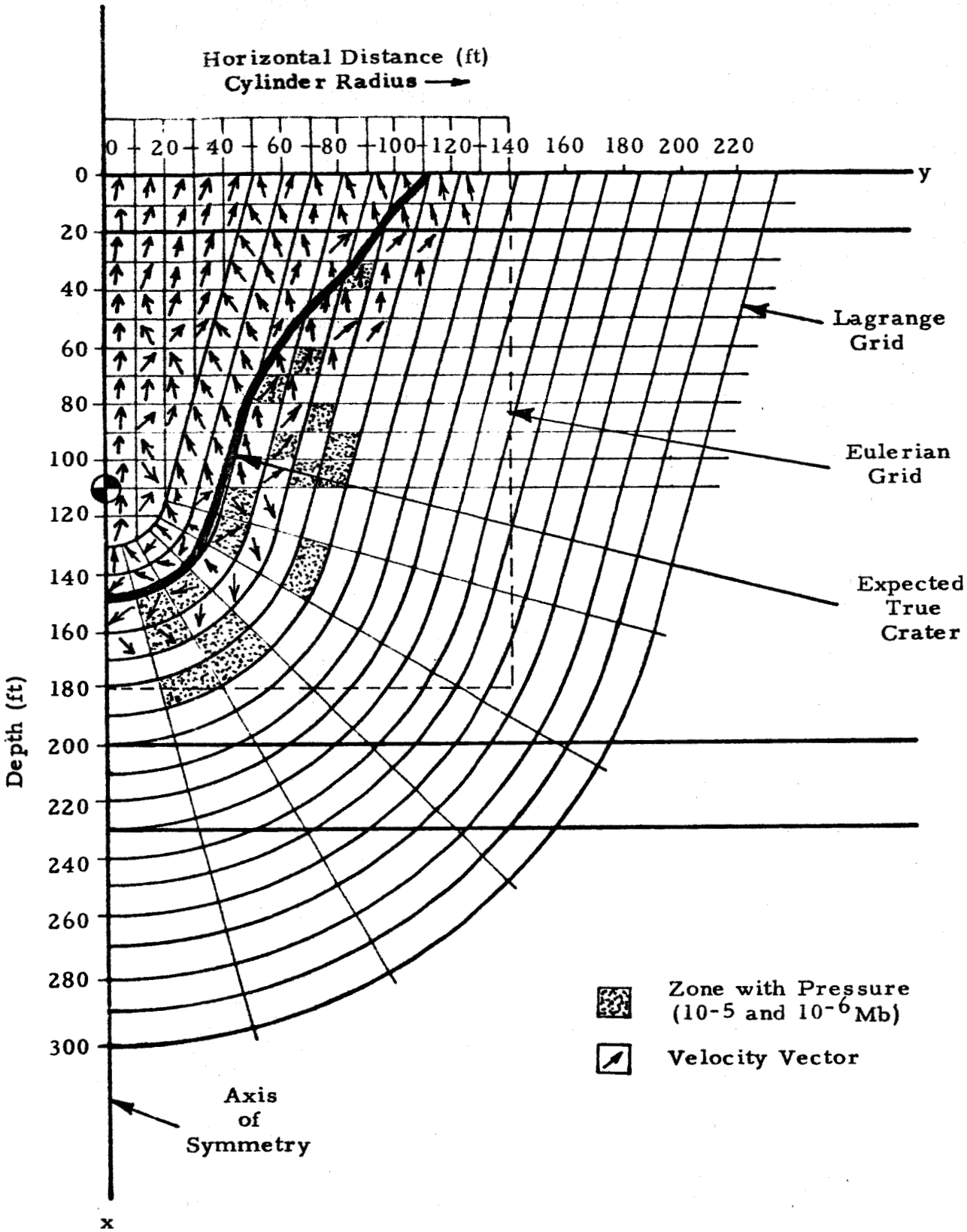

FIGURE 16. FORMATION OF DANNY BOY CRATER, Time = 30,359 μsec

B. ALUMINUM IMPACT CALCULATION

1. Background

The aluminum impact problem dealt with a 1-cm diameter aluminum sphere impacting an aluminum half space at an impact velocity of 7.32 km/sec (~24,000 ft/sec). The purpose of the problem was to see if computer computations simulating the cratering phenomena could predict depth-of-pentration results determined experimentally.

The type of aluminum considered in the calculation was an 1100 series aluminum. The statically determined tensile strength of this series is approximately 1 kb. Hypervelocity impact testing of the 1100 series (Ref. 13) has found that spall is incipient at approximately 10 kb.

The calculation was compared to the experimental results reported in Reference 14. In this experiment aluminum spheres of various diameters were launched into aluminum targets at different impact velocities. The depth of penetration was recorded and the ratio of penetration depth to sphere diameter was plotted against impact velocity. Figure 17 is a copy of this plot. It can be seen that a 1-cm sphere at 7.32 km/sec will penetrate approximately 3 cm into the target.

2. Problem Set-Up

The problem was calculated in two stages. The first stage involved the time from the initial impact to the time when the maximum stress in the target reached approximately 180 kb. The assumption was made that this stage of the calculation did not need the strength properties of the aluminum; it was therefore computed entirely in an Eulerian coordinate system. The second stage began where the first stage ended and was used for the remainder of the problem. The distinguishing characteristic of the second stage was the presence of a Lagrange grid in the region where the target would experience maximum stress levels less than 100 kb.

Figure 18 shows the Euler grid that was used in the beginning of the first stage. When activity neared its boundaries, the grid was dezoned

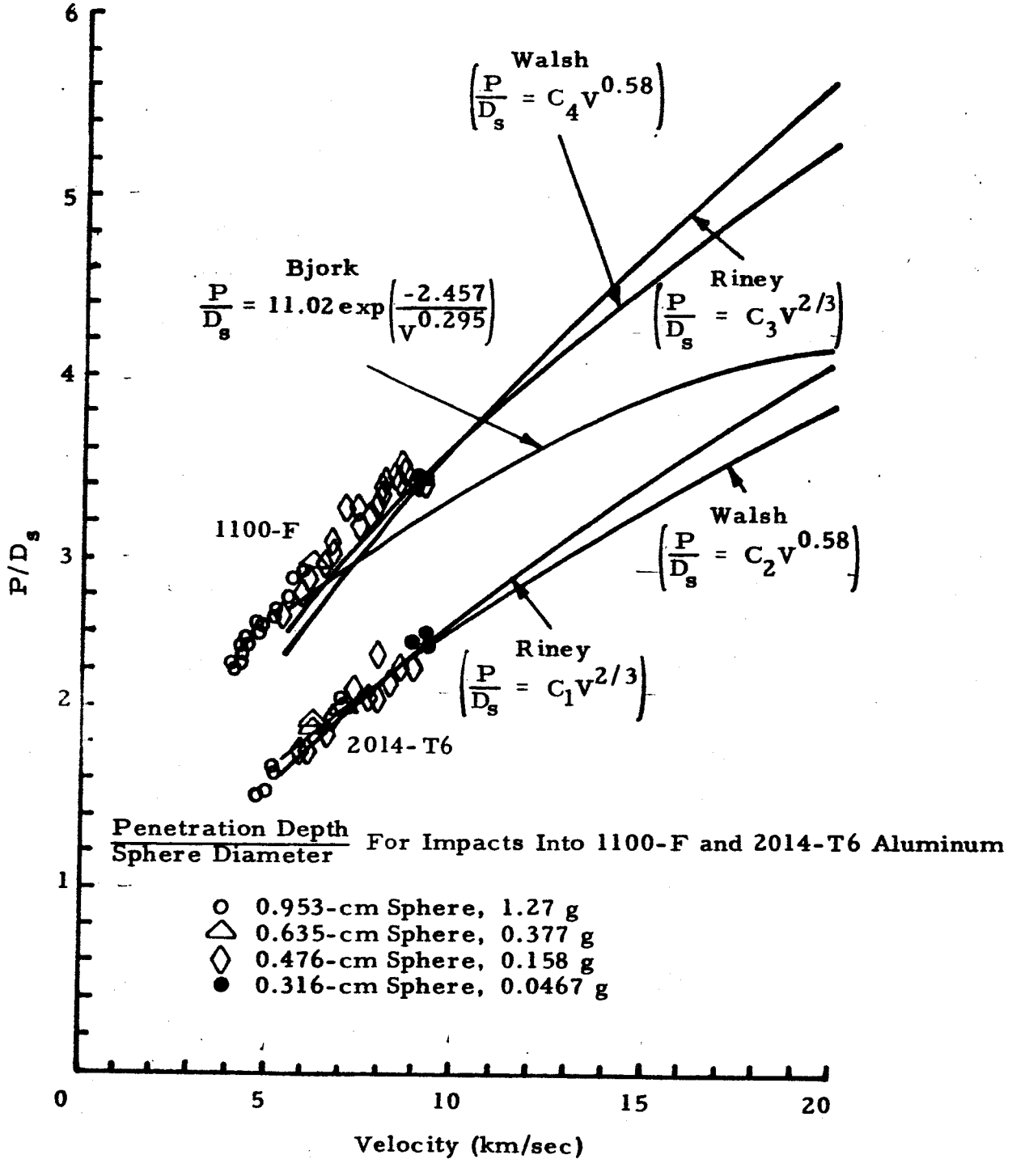

FIGURE 17. DIMENSIONLESS PENETRATION RATIO VERSUS VELOCITY FOR IMPACTS INTO 1100-F and 2014-T6 ALUMINUM BY 2017 ALUMINUM SPHERE (Figure from Reference 14)

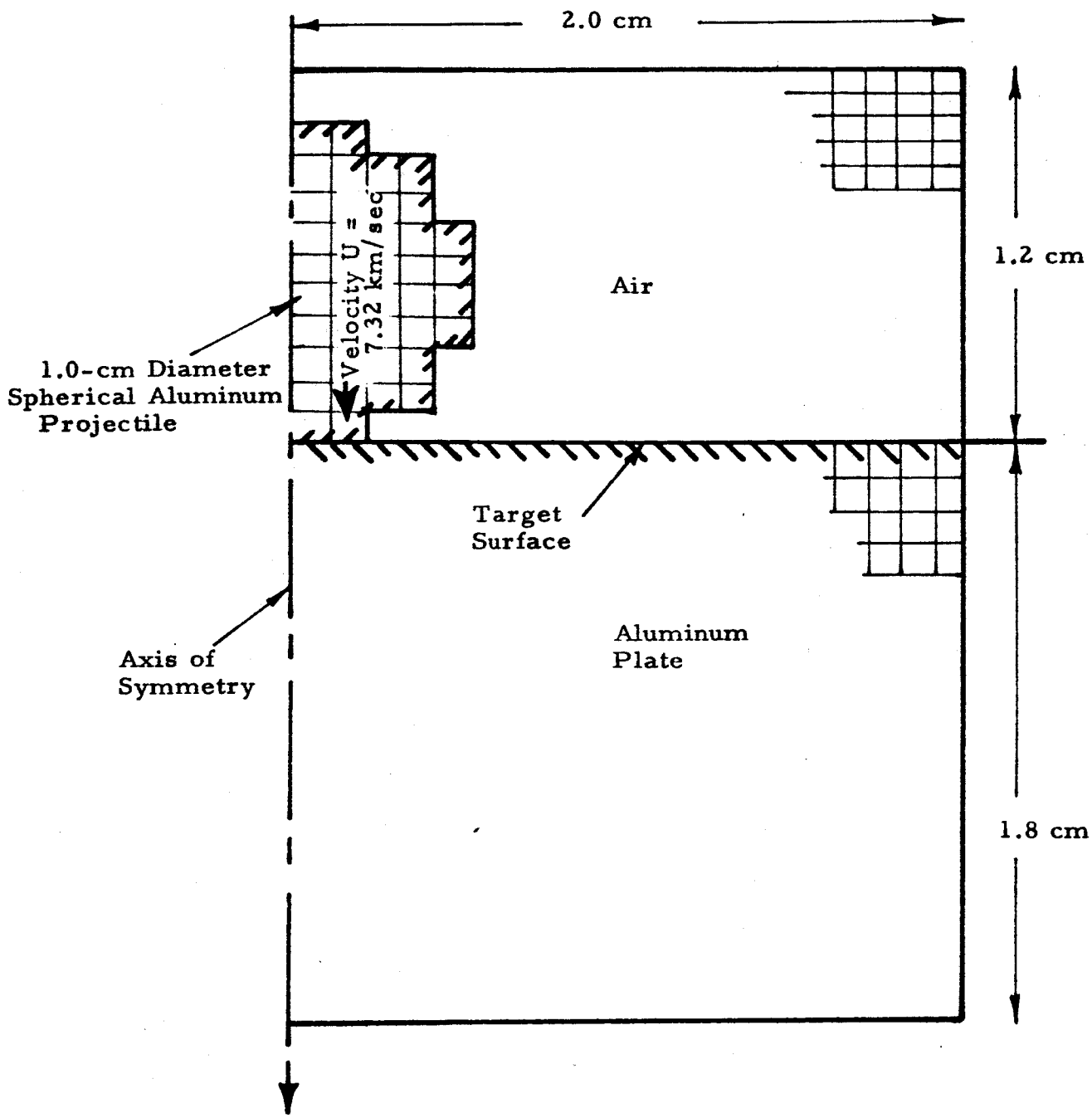

FIGURE 18. ORIGINAL GRID, BEFORE DEZONING AND BEFORE THE INTRODUCTION OF A LAGRANGE GRID

to a size exactly twice that shown in Figure 18. In both the original and dezoned grids the x-axis is the line of impact of the projectile, while the y-axis represents the surface of the target. Thus the x-axis is also the axis of symmetry of the problem.

The spherical projectile, composed of 0.1-cm-square aluminum zones, was given at impact time an initial kinetic energy consistent with the 7.32 km/sec impact velocity. The target, also composed of 0.1-cm-square aluminum zones, had no initial energy at impact time. (An interesting side note is that the air actually was treated as aluminum vapor. The Euler grid accepts only one equation of state for a calculation. Thus the only distinction that could be made was to give the aluminum in the region designated as air a density of 0.001 g/cm^3.)

By the time dezoning took place the maximum pressure in the target had decreased from over a megabar at the time of the impact to approximately 340 kb; the projectile had become completely fluid; and the shock was defined by several zones. All of these conditions were necessary so that no important detail was smeared out in the dezoning process.

The second stage began after pressure attenuation in the dezoned Euler grid had lowered the maximum stress in the target to approximately 180 kb. A polar-type Lagrange grid was laid over the dezoned Euler grid in the manner shown in Figure 19. Material in the uncovered Euler grid was or would be shocked into a fluid state. Material in the Lagrange grid, on the other hand, could become fluid or could remain solid. It was expected that the Lagrange grid closest to the impact point would move outward, uncovering Eulerian cells (making the material fluid), stopping short of the region where the true crater was expected to form. The location of decompressed zones and the direction and magnitude of the material velocity field in the Lagrange grid would then be considered in order to define the crater.

The aluminum equation of state throughout the entire problem was defined by a polynomial of the form

$$P = 0.79\mu + 1.51\mu^2 + 0.3\frac{E}{V}, \quad \mu = \frac{1}{V} - 1.$$

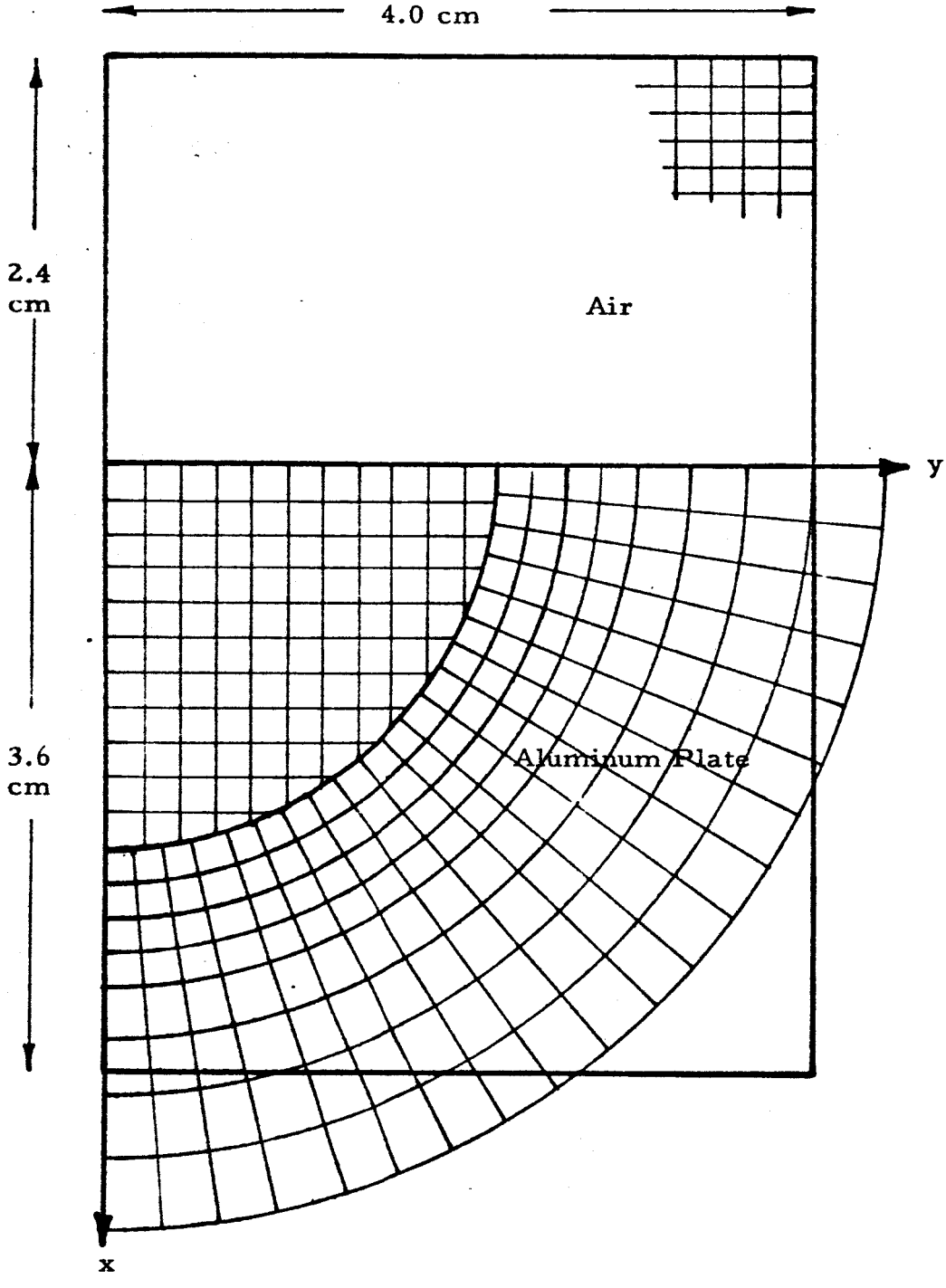

FIGURE 19. FINAL GRID SHOWING THE LAGRANGE GRID WITH RESPECT TO DEZONED EULER GRID

In addition, a von Mises yield stress of 1 kb and a shear modulus of 0.275 Mb were imposed.

3. Results

Figure 20 shows the shape of the crater after 6.49 μsec. The shock produced at impact time (t = 0) has traveled approximately 5 cm. Penetration depth is seen to be approximately 1.5 cm. All the material below the crater line has a density greater than or equal to the normal density of aluminum. The Euler-Lagrange interface line presently located in this region had originally been placed at a radius 2.2 cm from the point of impact. Its present position indicates it has moved over 0.1 cm. The velocity vectors above the crater line lie in a region where the density drops off from approximately 2.7 g/cm^3 at the crater line to approximately 0.25 g/cm^3 at the end of this region. Beyond this, practically no aluminum exists and no velocity vectors are plotted. The mass formerly occupying this volume has become ejecta.

Figure 21 is identical in format to Figure 20 explained above. The time here is 21.63 μsec, and the shock has traveled to a distance of 12.5 cm. The penetration depth is approximately 2.8 cm, and the crater and Euler-Lagrange interface lines are very close together. Pressures around the crater line have diminished from 10 to 15 kb in Figure 20 to about 2 to 3 kb. Since the yield strength of the aluminum is about 1 kb, it is not expected that the crater will get much larger. This is supported by the low magnitude and direction of the particle velocities. It appears as if the expected penetration depth of 3.0 cm is exactly what the calculation would reach if the problem were continued to a later time.

As a check on the accuracy of the two-dimensional calculation and equation of state, a plot of peak maximum stress versus radial distance from impact, Figure 22, was made to compare the calculated values with experimental results reported in Reference 13. The agreement is excellent up to a scaled radius of about 1.5 cm. Beyond this point the initial radial zone size in the calculation was determined by a geometric progression that made each zone 10 per cent larger than its

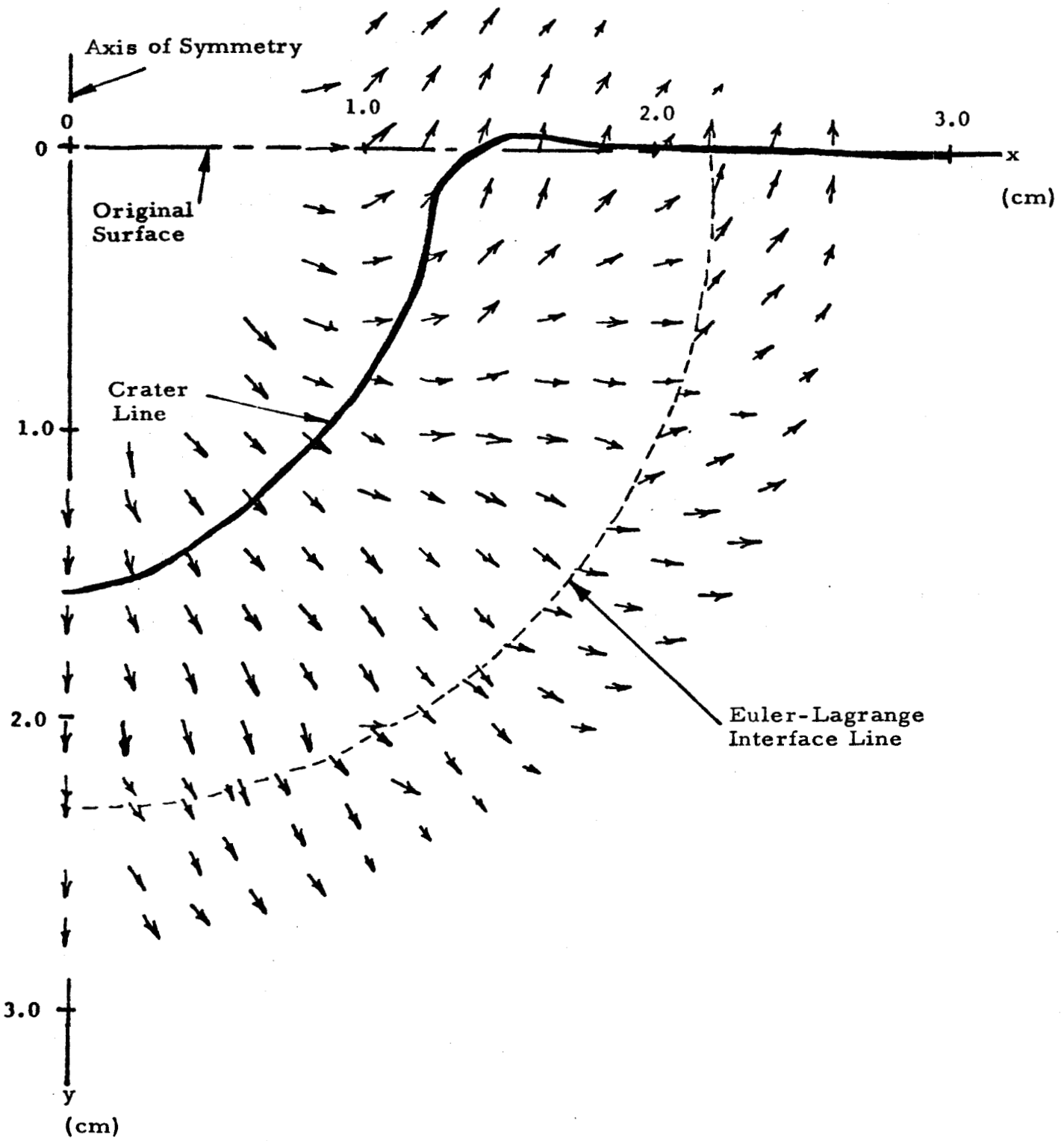

FIGURE 20. ALUMINUM IMPACT PROBLEM,
Time = 6.49 μsec

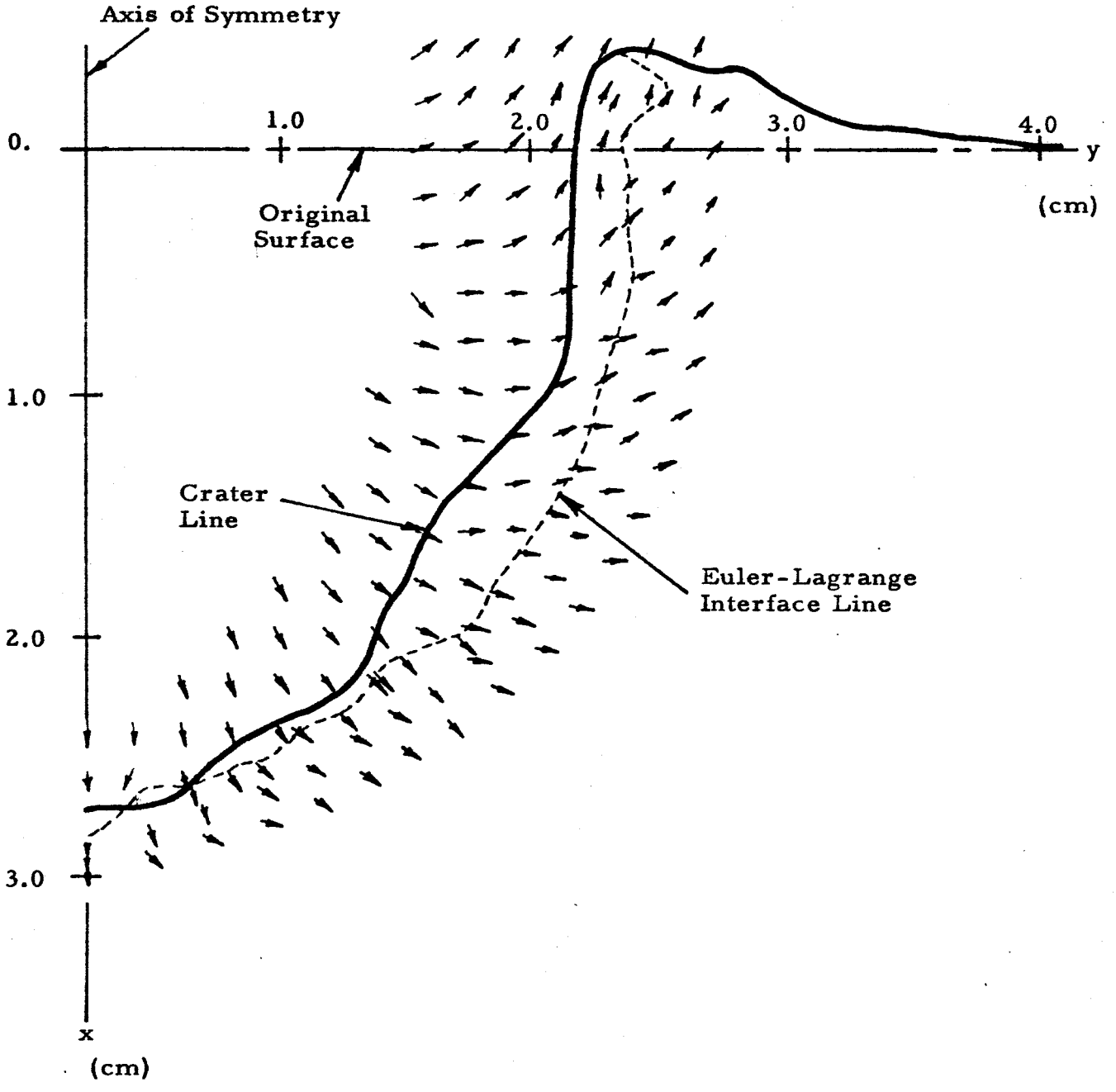

FIGURE 21. ALUMINUM IMPACT PROBLEM,
Time = 21.63 μsec

2022

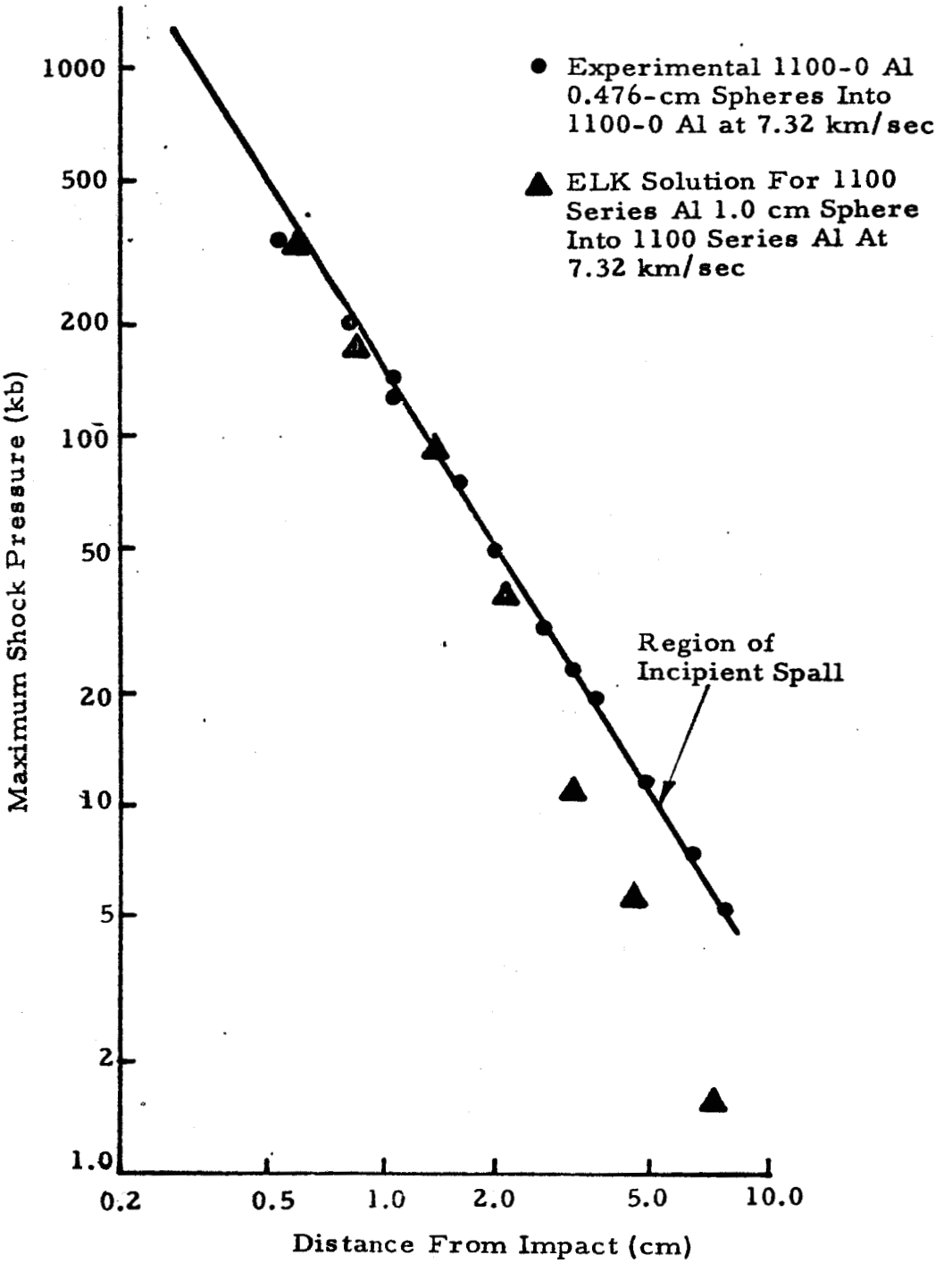

FIGURE 22. CALCULATED AND MEASURED MAXIMUM SHOCK-WAVE PRESSURES GENERATED BY IMPACTS OF EQUIVOLUME PROJECTILES INTO 1100-0 ALUMINUM TARGETS

neighbor radially closer to the source. This was done to conserve machine time. The effect of larger zones tends to smear out peak values. However, the larger zones were far enough from the crater region so that they had no effect on the crater formation. It is apparent that if the initial radial zone size had been equal to that used in the crater region, the agreement in Figure 22 would have been excellent everywhere. The advantage in this respect of applying a coupled code with a Lagrange grid describing material strength for low stress is obvious. Up till now only pure Eulerian codes could handle the calculation where peak pressures were above 100 kb.

Experience gained in this problem indicates two improvements that could be made in any subsequent aluminum impact runs. First, noise in the Eulerian calculation could be significantly reduced by the application of an artificial viscosity. A smoother-looking pulse shape at early times would allow more detailed analysis at late times. Originally it was felt that the viscosity inherent in the Eulerian finite difference equations was sufficient to give a smooth solution, but its effect turned out to be inadequate. Secondly, the crater would have been better defined if the crater line had ended up in the Lagrange grid. This could be accomplished by moving the Lagrange grid closer to the source. These two improvements should be accompanied by finer zoning.

C. AN INVESTIGATION OF TERRESTRIAL COMET IMPACTS AS AN ORIGIN OF TEKTITES

The hypothesis that tektites originated as the result of a cosmic body impacting the earth was suggested by Spencer (Ref. 15, 16). This suggestion has been modified and supported by Urey (Ref. 17, 18), Barnes (Ref. 19), Cohen (Ref. 20) and Gentner, et al (Ref. 21). An intensive investigation of the origin of tektites was conducted by Chapman and Larson (Ref. 22). They employed high-speed digital computers with analytical and experimental studies that apparently refute the terrestrial origin hypothesis. The study of this question at Physics International, reported here, was not intended to prove or disprove the terrestrial origin hypothesis; many of the objections given by Larson and Chapman are not considered. Rather, the objective was to

employ the calculational systems available in the Physics International impact and cratering codes and to examine the time-history of comet impacts in a mechanistic way, hoping to uncover some previously overlooked mechanisms that might have some bearing on the origin of tektites. Before reporting on the results of particular calculations, it is useful to envision a possible time sequence of events to serve as a framework for further discussion.

A giant comet composed of a brittle, lace-like conglomerate of frozen gas crystals penetrates the earth's atmosphere, forming a transient low-density "tunnel" in its wake. The comet impacts the earth's surface and drives inward for hundreds or thousands of meters, depending on the parameters of impact. The heat of impact vaporizes the comet and the earth material in the immediate vicinity. A large amount of earth material is melted, and a still larger amount is pulverized. The gases expand explosively outward and upward, followed by part of the wide spectrum of earth ejecta. A small number of the molten ejecta, launched at approximately 10 km/sec and subjected to the disrupting aerodynamic forces of the expanding gas, escape the atmosphere. Molten units of glassy material with masses of tens to hundreds of grams solidify into spheres as they travel in orbits covering a substantial fraction of the earth's circumference. In their final descent, these particles partially remelt and ablate in the earth's atmosphere, forming the characteristic ridges and flanges observed in tektites.

Chapman and Larson firmly reject this envisioned process. They show that a molten glassy sphere of 3-cm radius launched at the earth's surface cannot survive the disruptive aerodynamic forces unless the following (equivalent) conditions are met:

$$(1a) \quad \Delta P_{aero} < 2 \times 10^{-4} \text{ atm}$$

$$(1b) \quad \rho_\infty V_\infty^2 < 200 \text{ dynes/cm}^2$$

$$(1c) \quad a_{ccel} < 0.015 \text{ earth g}$$

ΔP_{aero} is the aerodynamic pressure differential between stagnation and base pressures; ρ_∞ is the ambient atmosphere density; V_∞ is the relative

velocity with respect to this atmosphere; a_{ccel} is the resulting tektite deceleration determined from (1a) and the tektite mass. These severe restrictions cannot be met unless (1) the atmosphere is essentially removed by a low-density tunnel left in the wake of the incoming comet, (2) the small outgoing molten spheres maintain a small relative velocity with respect to the expanding explosion gases, or (3) the small molten spheres are shed from larger parent bodies that do not completely disrupt before escaping the atmosphere. The mechanism for launching a more or less intact large body may be complex. This in itself does not preclude its existence in the very chaotic explosion configurations that are possible. Though it has not been done, it might be fruitful to find a class of accelerations that could launch a large body at 10 km/sec without destroying it immediately, and then see under what conditions this class of accelerations could exist after or during impact. For example, light-gas guns are used routinely to accelerate plastic projectiles without disruption up to speeds of roughly 10 km/sec. It would be shown that a vertically impacting comet essentially buries itself in the earth as it impacts and converts into gas. This gas, plus that released by ground moisture in the vicinity of the impact, represents a large potential for obtaining relatively slow, uniform accelerations of earth projectiles. It should be emphasized that this process does not correspond to a single shock followed by a rarefaction, which would disintegrate any earth projectile accelerated to 10 km/sec.

The tunnel hypothesis, whereby small molten tektites escape through a low-density tunnel in the atmosphere left in the comet wake (with no other process being invoked), does not survive analytical examination. A calculation that included the effects of air viscosity (Chapman, Ref. 23), indicates that the pressure in such a tunnel does not drop much below one-tenth of ambient pressure, and that the tunnel is closed effectively by the trailing shock wave of the comet after a few diameters of distance. Godfrey, Andrews, and Trigg (Ref. 24) confirm this result in a particular two-dimensional code calculation of a giant comet. In this calculation, a large comet with density 0.01 g/cm^3,

radius 5 km, and a speed of 40 km/sec enters the earth's atmosphere vertically and collides with the earth's surface. This calculation shows the transient tunnel diameter to be very close to the comet diameter.

It is clear from solid-angle considerations that vertical or nearly vertical comet impacts are relatively improbable. It is unfortunate that this is the only geometry that can be applied correctly in a two-dimensional code calculation. The energy and momentum going into earth ejecta from a vertical comet impact would be small compared to those obtained from a shallow-angle impact. The two-dimensional plane (or translational) geometry of Figure 23 can be applied to mock up nonvertical impacts. It would be interesting to determine the energy and momentum enhancement in the ejecta of this geometry. Impacts at shallow angles should be particularly effective in ejecting large masses of earth material, perhaps producing the large parent bodies postulated earlier.

From this discussion, it is clear that the present calculational program is far from complete. To date a variety of code calculations have been made, of which representative ones will be discussed.

1. One-Dimensional Impact Calculations

Since the terrestrial origin hypothesis is in disfavor, it was decided to give it every advantage in the choice of initial conditions for the one-dimensional calculations. This is done by assuming very large incoming comets. A comet density of approximately 0.3 g/cm^3 was chosen. The comet gas equation of state with γ equal to 1.4 was chosen to match that of air, for purposes of normalizing for a later two-dimensional calculation. The crystalline comet equation of state before impact enters into the impact in a very insensitive way. The reflected shock from impact converts the comet crystals into gas. The gas properties dominate the expansion after impact. Gamma values as low as 1.2 have been used for the comet gas equation of state in code calculations with no important changes in the behavior of the explosion and expansion. A granite earth was chosen for all of the code calculations, with a Tillotson formulation for the equation of state. This choice is

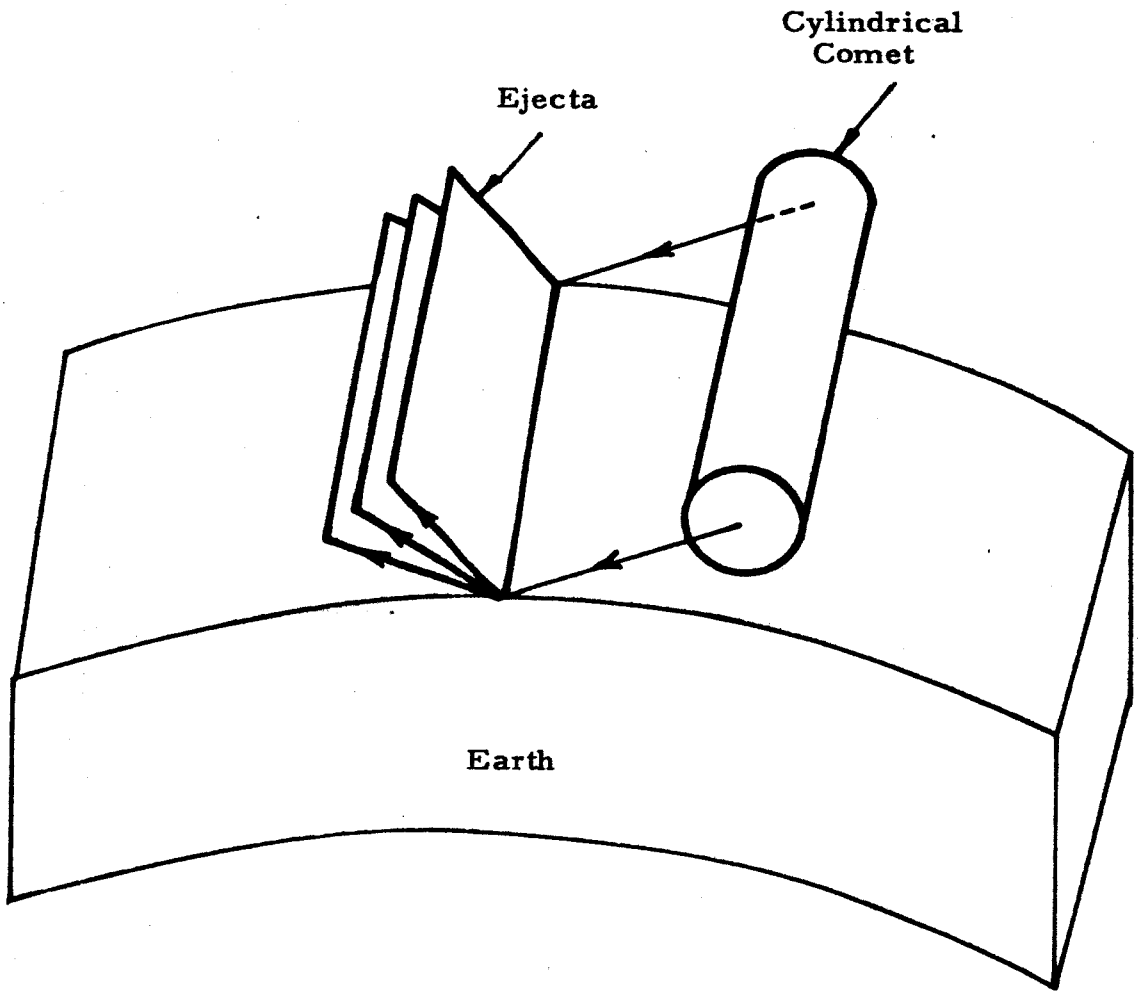

FIGURE 23. TWO-DIMENSIONAL APPROXIMATION OF OBLIQUE IMPACT OF A LARGE COMET ON EARTH'S SURFACE

more closely normalized to experiment than are other possible candidates. The details of this formulation are not given here, except to note that one of the coefficients in this equation of state was changed from a value of 0.5 to 0.4. This had the effect of changing the effective gamma of hot granite vapor from 1.5 to 1.4, again for reasons of normalizing to later two-dimensional calculations. The principal Hugoniot curves for this granite are given in Figures 24, 25, and 26.

FLUDOC Linear Comet No. 4 had the initial configuration shown in Figure 27. It should be emphasized that all motion is linear and that no side rarefactions are possible in this calculation. Figure 28 shows the height-time trajectories of the comet zonal boundaries. The boundary at the earth-comet interface is seen to retreat to a depth of approximately 1.4 km before moving back to about 1-km depth at 1 sec. This problem was not continued long enough to make an estimate of the final crater depth, which of course is not meaningful in a one-dimensional calculation. The important feature here is that the comet essentially buries itself in the granite earth before exploding. The retreating earth, undergoing unavoidable Taylor instability, is a rich source of debris that is distributed in the imbedded comet at $t \tilde{=} 0.10$ sec. Two-dimensional effects would bring in another source of debris by the process of Helmholtz instability, or "wiping." In any case, the expanding comet gas after a period of violent acceleration expands more or less uniformly after 0.5 sec with a spectrum of velocities. It will be seen later in similar conditions that the atmosphere substantially slows up this expansion at later times.

The distribution of debris in a finely zoned version of the geometry of Figure 27 for $t \leq 0.1$ sec was calculated on the Physics International INSTAB code. This code calculates the usual Taylor instability growth for inviscid fluids and couples in "bubble" and "spike" stage logic in a phenomenological way to find the final distribution of the debris. Figure 29 shows the domains of debris particles, size versus position. This calculation neglects the viscous drag that would tend to sweep the smaller particles downward. This effect could be calculated with some

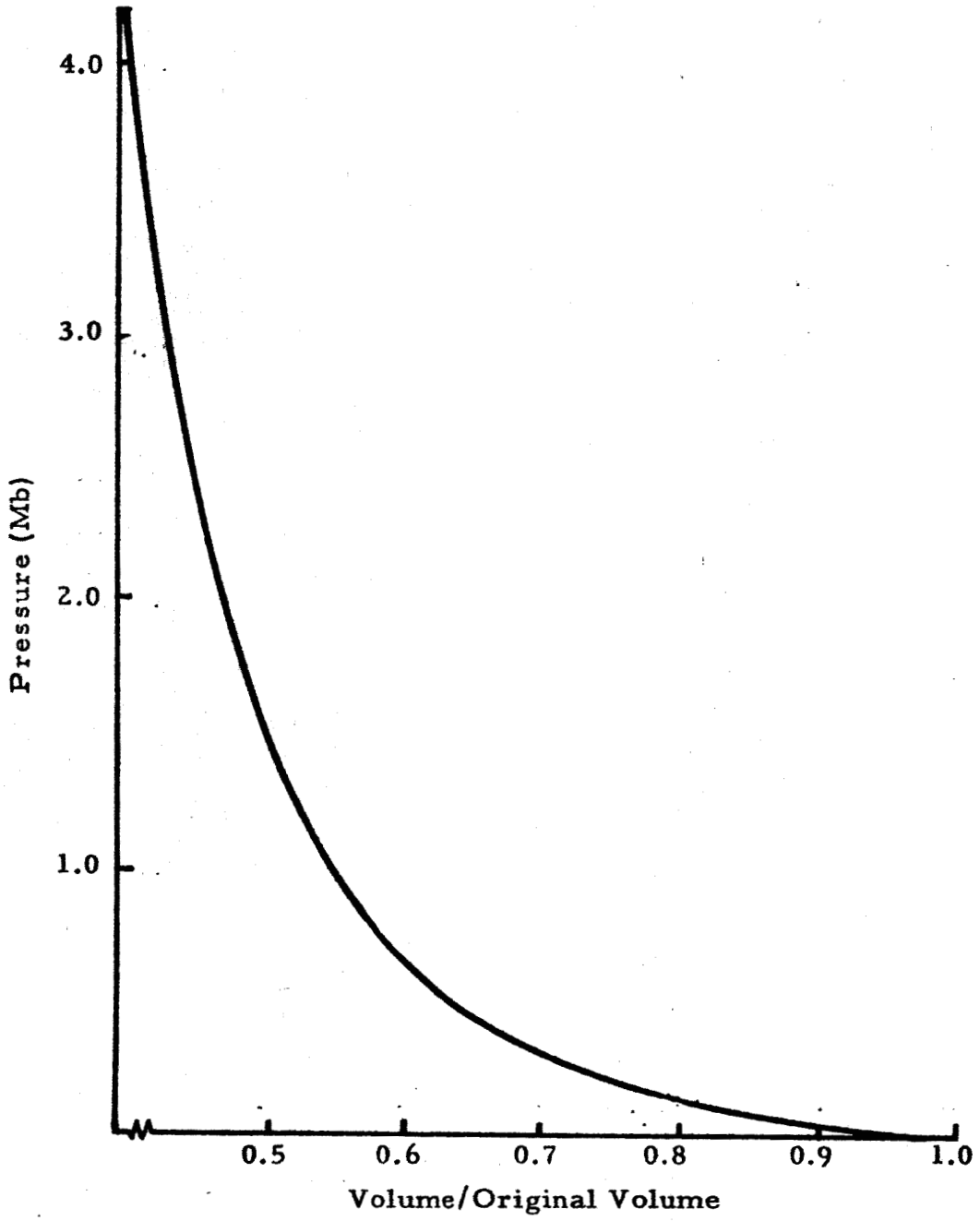

FIGURE 24. PRINCIPAL HUGONIOT FOR GRANITE, PRESSURE VERSUS RELATIVE VOLUME (ρ_o granite = 2.65 g/cm^{-3})

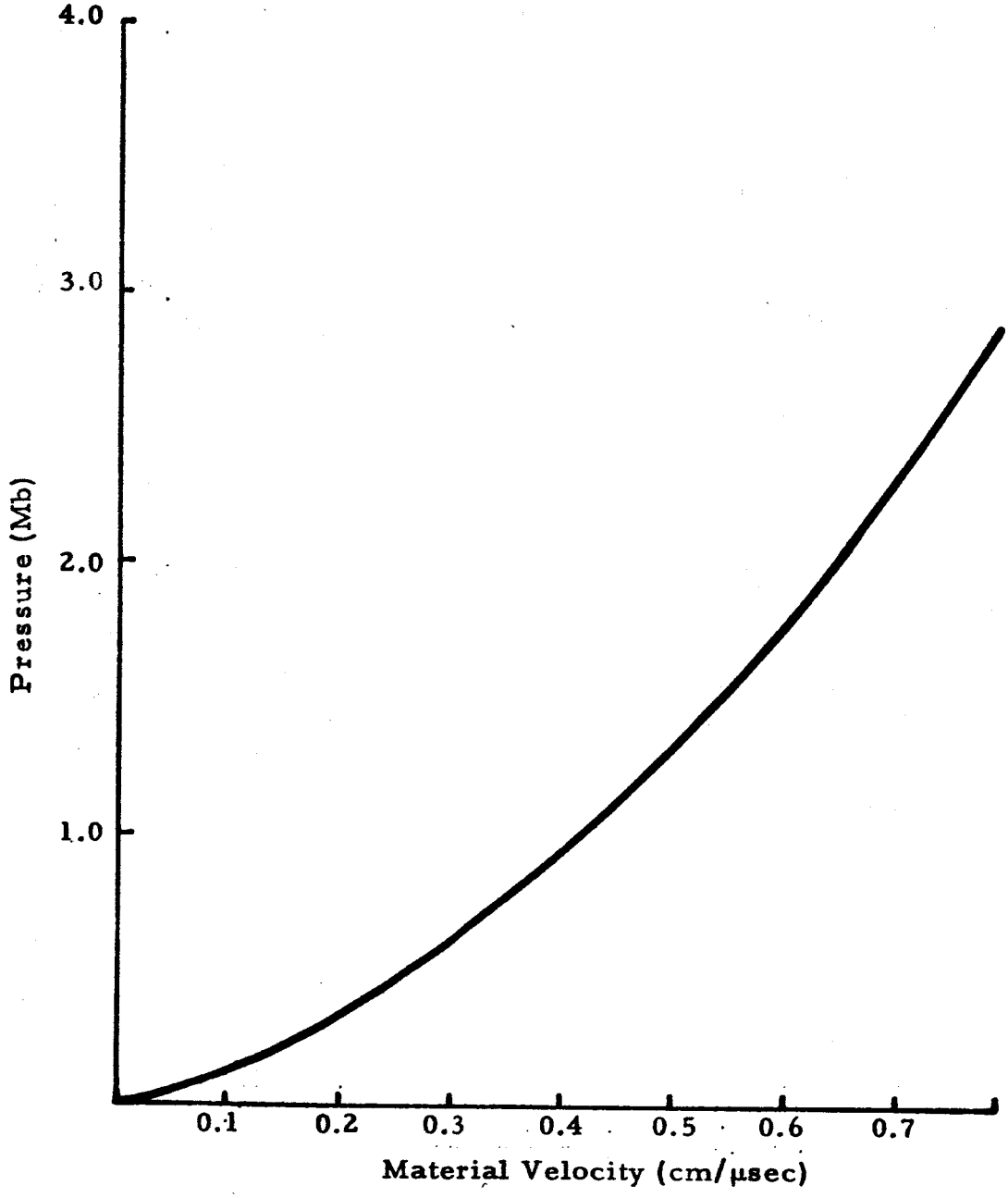

FIGURE 25. PRINCIPAL HUGONIOT FOR GRANITE, PRESSURE VERSUS MATERIAL VELOCITY

2028

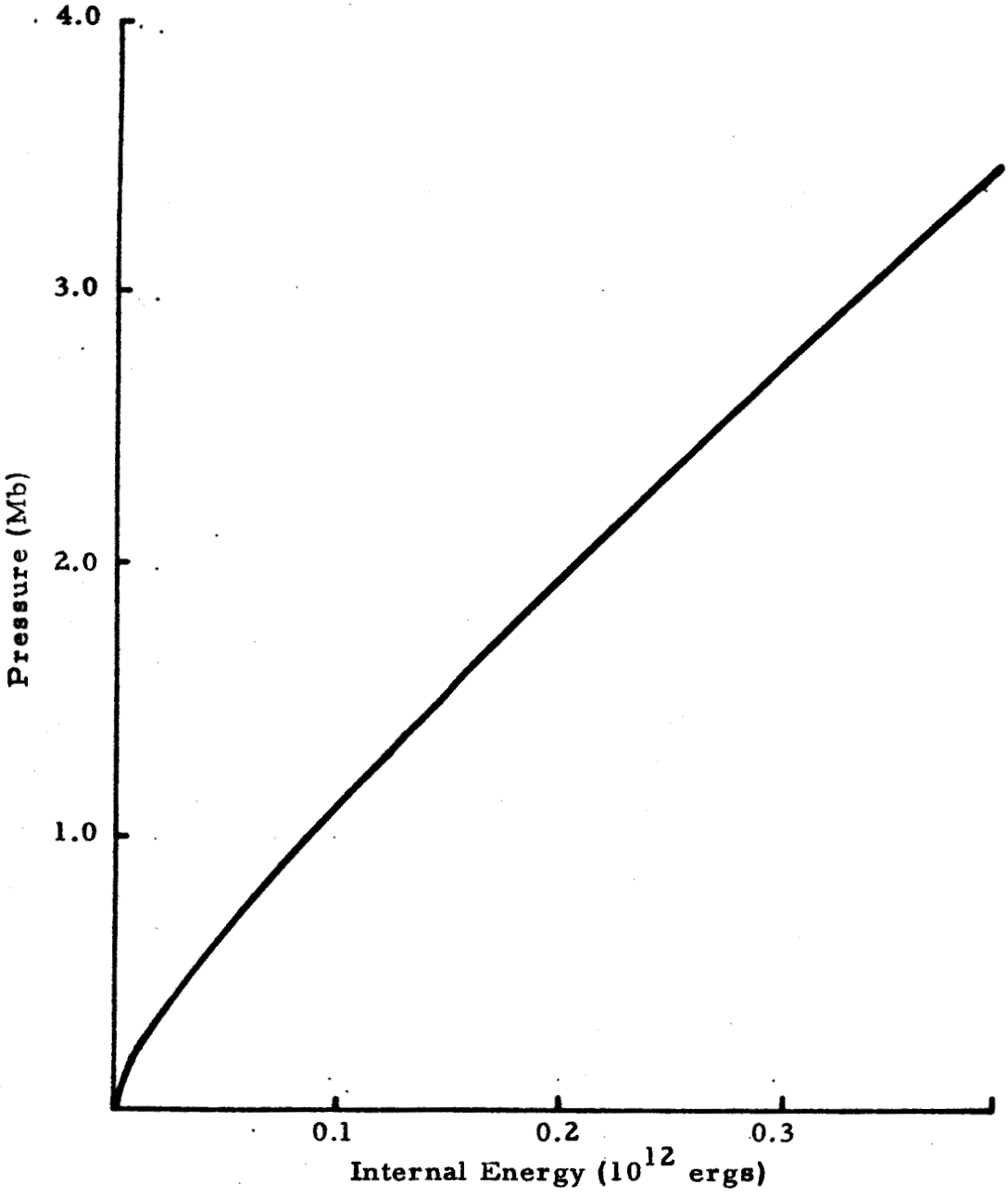

FIGURE 26. PRINCIPAL HUGONIOT FOR GRANITE, PRESSURE VERSUS INTERNAL ENERGY

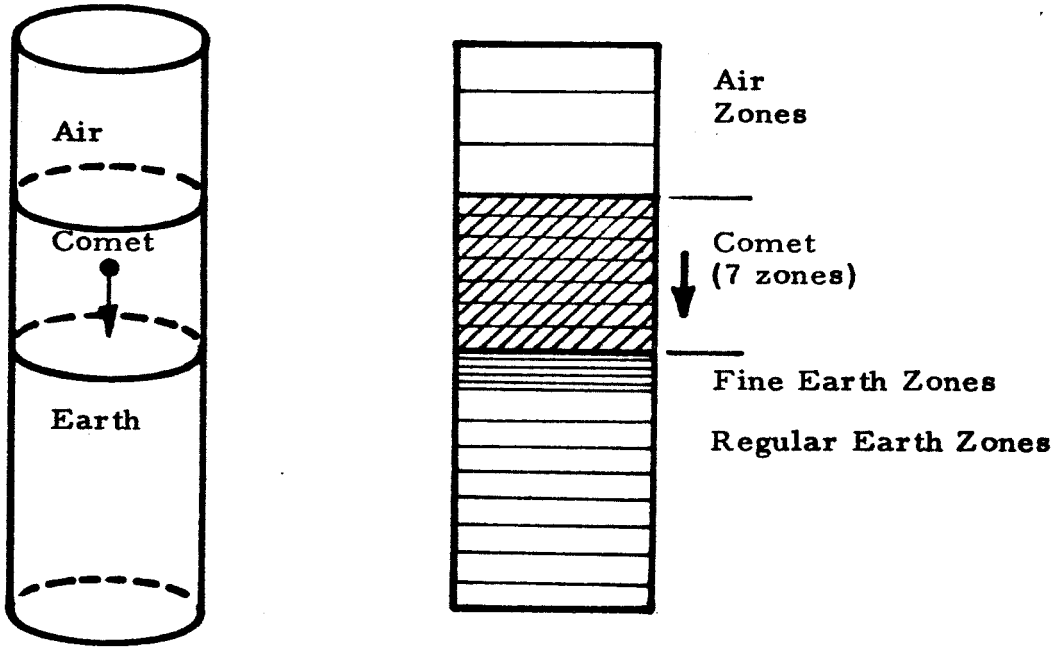

FIGURE 27. INITIAL CONFIGURATION FOR CALCULATION OF LINEAR COMET NO. 4

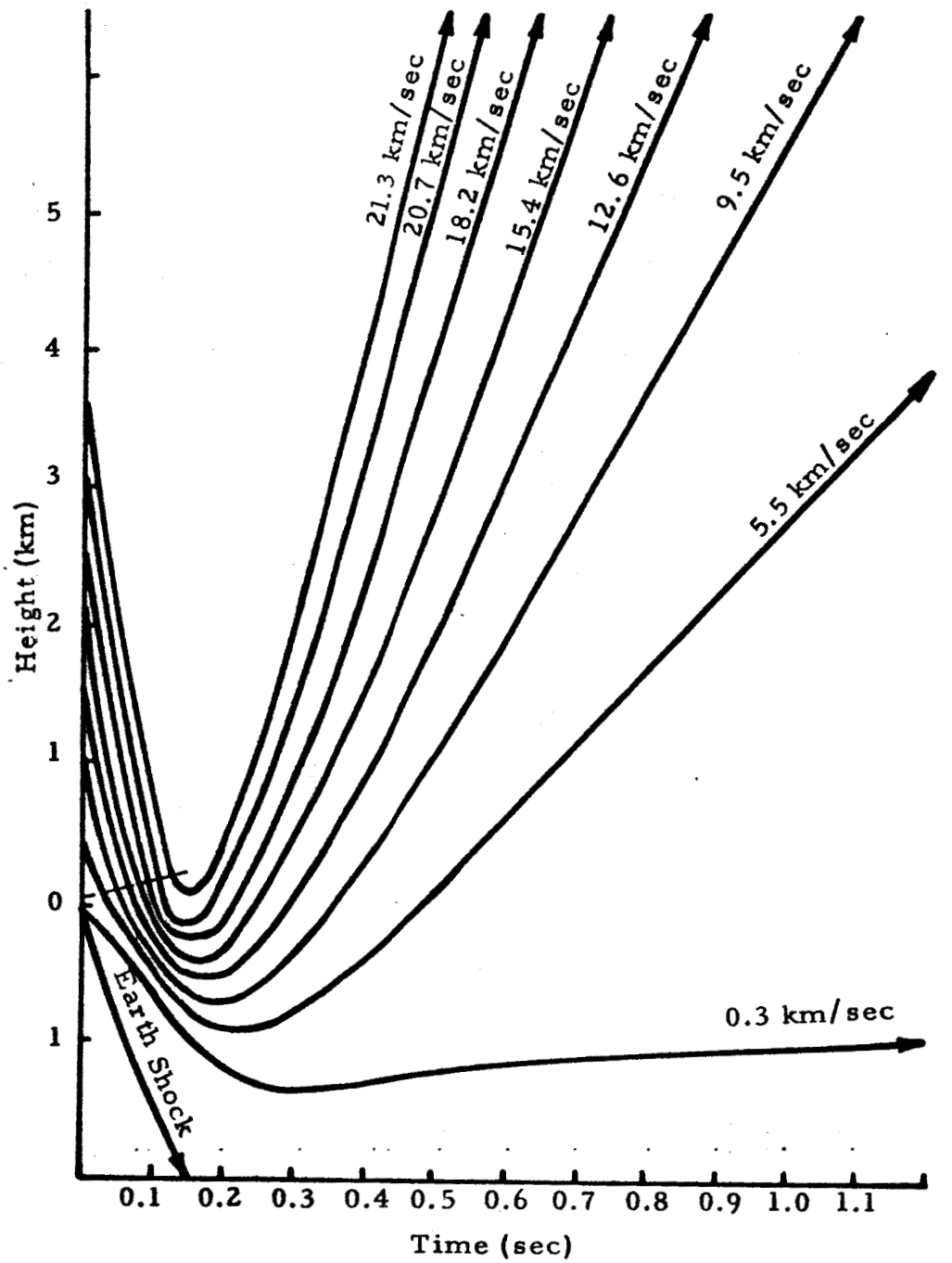

FIGURE 28. HEIGHT-TIME TRAJECTORIES FOR ZONAL BOUNDARIES OF CALCULATED LINEAR COMET NO. 4

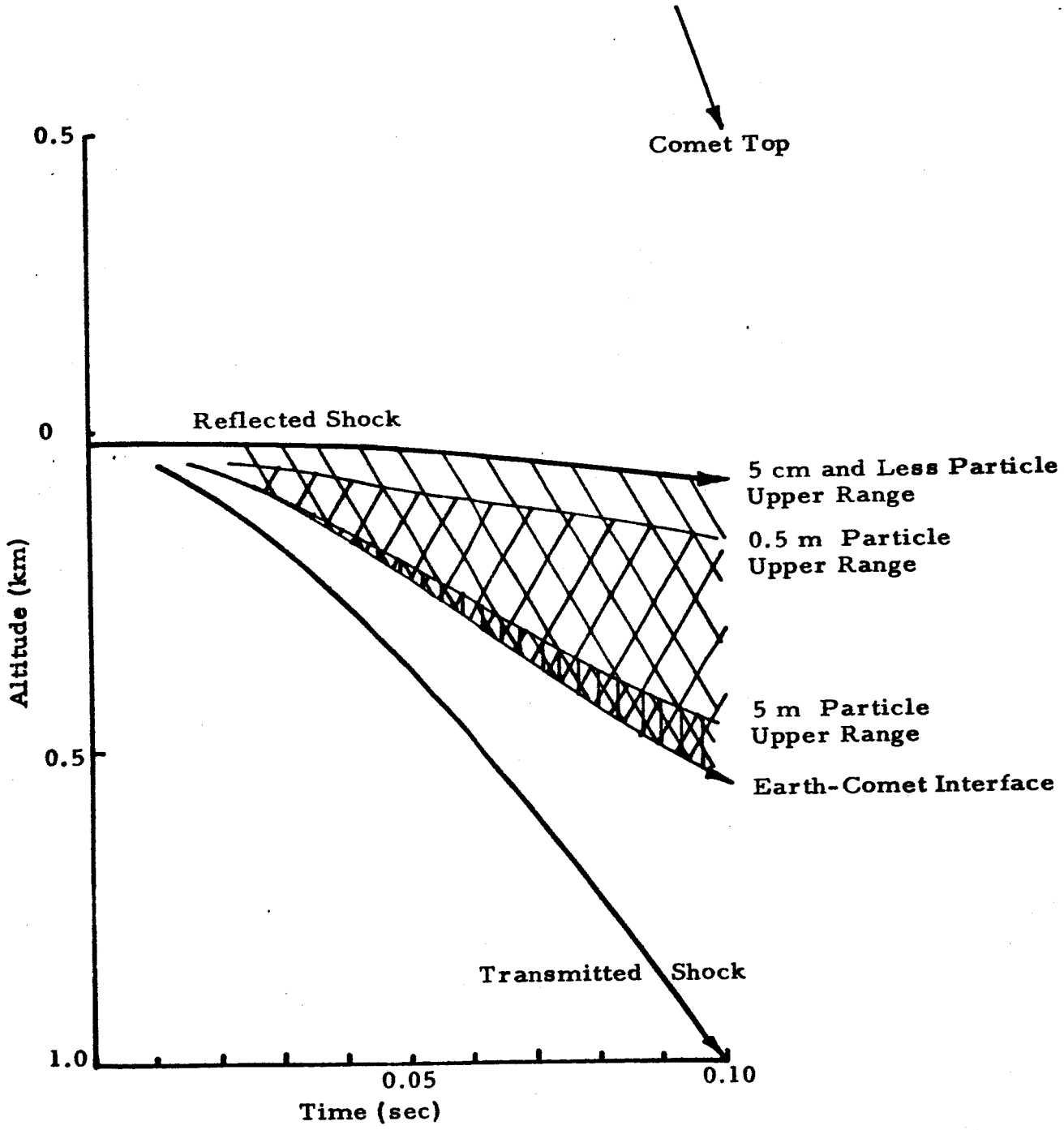

FIGURE 29. FINAL DISTRIBUTION OF DEBRIS, CALCULATION OF LINEAR COMET NO. 4

effort on the Physics International PARDOC code. This code allows one to introduce a spectrum of spherical particles into the spatial coordinates of a standard one-and-one-half dimensional hydrodynamic code; these particles are then accelerated by the viscous drag forces as the hydrodynamic calculation proceeds. It is thought, however, that the large-scale vorticity and chaotic nature of this violent impact cannot be calculated in detail by any code. The important point is established, however. The exploding comet is permeated with a large mass of earth material dispersed over a wide spectrum of sizes and positions. In the chaotic aftermath following impact it may be possible to find selective mechanisms that launch a small fraction of the debris bodies in solid or liquid phase with escape velocity. Certainly most of them would explode when the expansion rarefaction relieves the megabar pressures and explodes any inclusions of water or volatile material. The scarcity of these materials in the moon's crust makes a lunar impact much less susceptible to this phenomenon.

2. One-and-One-Half Dimensional Comet Impact Calculations

A series of one-and-one-half-dimensional comet impact computations were performed to (1) establish the starting conditions of a two-dimensional calculation and (2) examine the question of atmospheric blow-off by the expanding comet gas. The one-and-one-half-dimensional geometry is shown schematically below.

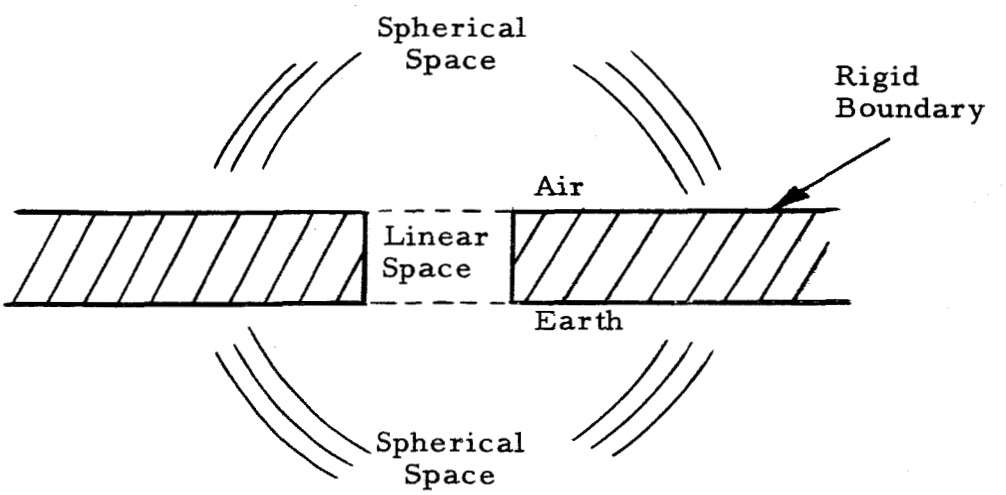

The flow cross-sectional area is constant in the linear region containing the original comet. Elsewhere the area is defined by an appropriate function of the single space coordinate to establish spherical geometry. No sidewards rarefaction is allowed in the linear space, an unavoidable condition of this geometry. Elsewhere, this model is approximately correct.

The comet was chosen to be a perfect gas with a gamma of 1.2, having an initial velocity of 30 km/sec. The air and granite earth equations of state were chosen as before. Three comet sizes were picked; these are described as follows:

Problem Name	Comet Radius (km)	Comet Height (km)	Comet Mass (10^{15} g)	Comet Kinetic Energy (10^{27} ergs)
A2	0.5	1	0.2355	1.06
B2	1.0	2	1.884	8.50
C2	2.0	4	15.12	68.00

The exponential atmosphere was approximated with four constant-density regions. These are shown in the table below.

No. Air Layer	Top Radius (km)	Density	Pressure (atm)	Mass (10^{15} g)
1	88	0.95×10^{-6}	0.0095	1.22
2	44	0.28×10^{-4}	0.0282	4.48
3	22	0.177×10^{-3}	0.177	3.63
4	11	0.704×10^{-3}	0.704	2.00

The calculation showed that the earth of problems A2 and B2 absorbed 64 per cent of the total energy, while in problem C2 this became 80 per cent. This nonscalable effect is not understood. It may result from the fact that the comet mass is small compared to that of the atmosphere in problems A2 and B2, and is not in problem C2.

The outgoing comet particle velocities were somewhat erratic. This effect is thought to have originated from the non-real density

discontinuities between the constant air layer regions used to mock up a graded atmosphere. In hindsight, it would have been preferable to rewrite part of the FLUDOC code to accept a realistically graded atmosphere. Rather than plotting the velocity-time history of various comet zones in the manner of Figure 28, it was necessary to plot the mean velocity-time history of Air Region No. 4 (above the comet). In spite of this, non-real oscillations appear. The results are shown in Figure 30 for Comets A2, B2, and C2. The dashed line estimates the behavior that would occur in an exponentially graded atmosphere. A severe deceleration appears in all cases. Clearly Comets A2 and B2 do not blow off the atmosphere, and Comet C2 does. The final upswing in the velocity of case C2 is due to the rarefaction from outer space converting the air's residual internal energy into kinetic energy.

This series of one-and-one-half-dimensional calculations indicates that a comet impact with about one million tons of incident kinetic energy (42×10^{27} ergs) is necessary to blow off a sector of the earth's atmosphere. Even so, an appreciable deceleration will exist in the early stages. The two-dimensional comet energy (38.8×10^{27} ergs) was chosen as an intermediate case between that of B2 and C2. As expected, the sidewards rarefaction during the two-dimensional impact degrades the comet gas expansion velocities somewhat more than the mean between B2 and C2 of Figure 30. It will be seen that the general features are quite similar.

3. Two-Dimensional Comet Explosion Calculation

This problem had the original configuration shown in Figure 31. The total energy of 38.8×10^{27} ergs corresponds to that of a spherical comet of radius 1.87 km, density 0.316 g/cm^3, with an initial velocity of 30 km/sec. This comet then is intermediate between that of C2 and B2 in the one-and-one-half-dimensional calculations. The two-dimensional computation was done on the ELK code in a pure Eulerian grid. This was thought to be necessary because of the violent flow in the regions of interest. In hindsight, it might have been better to employ coupled Eulerian-Lagrangian grids to eliminate the fictitious diffusion of earth and air along the earth-air interface. This fictitious diffusion, inherent

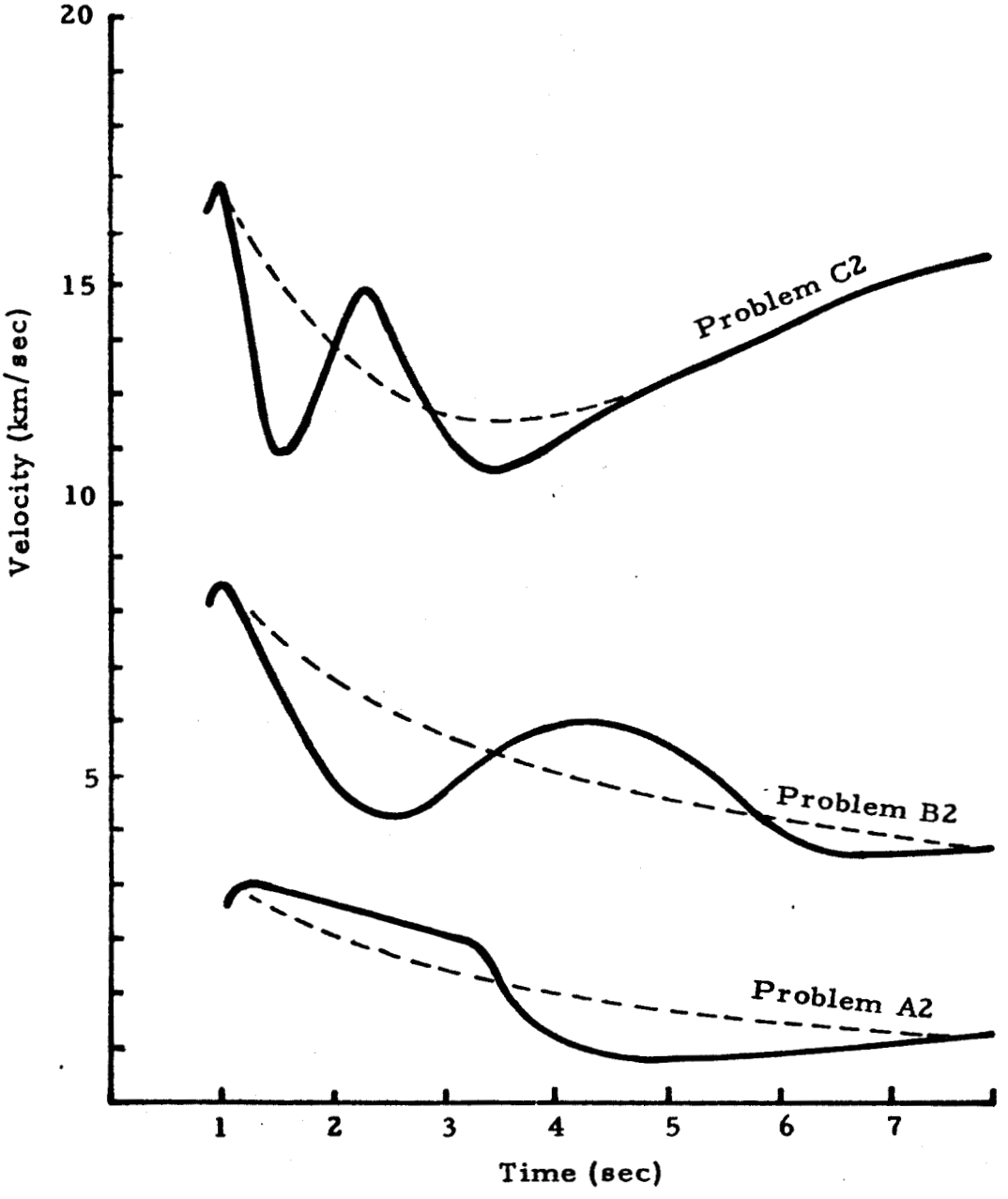

FIGURE 30. MEAN VELOCITY OF AIR LAYER NO. 4
(Directly Above Comet Gas)

Region	ρ	P (Mb)	$\dot{x}$ (km/sec)	$\dot{y}$ (km/sec)	
3	3.64	0.4145	0	3.0	
4	4.62	1.027	0	4.0	Shocked Earth
5	5.26	2.03	4.57	4.57	
6	5.26	2.03	6.46	0	
7	1.236	1.588	0	4	
8	1.236	1.588	2.83	2.83	Compressed Comet (γ = 1.4)
9	1.236	1.588	4.65	0	
10	1.236	1.588	1.31	0	

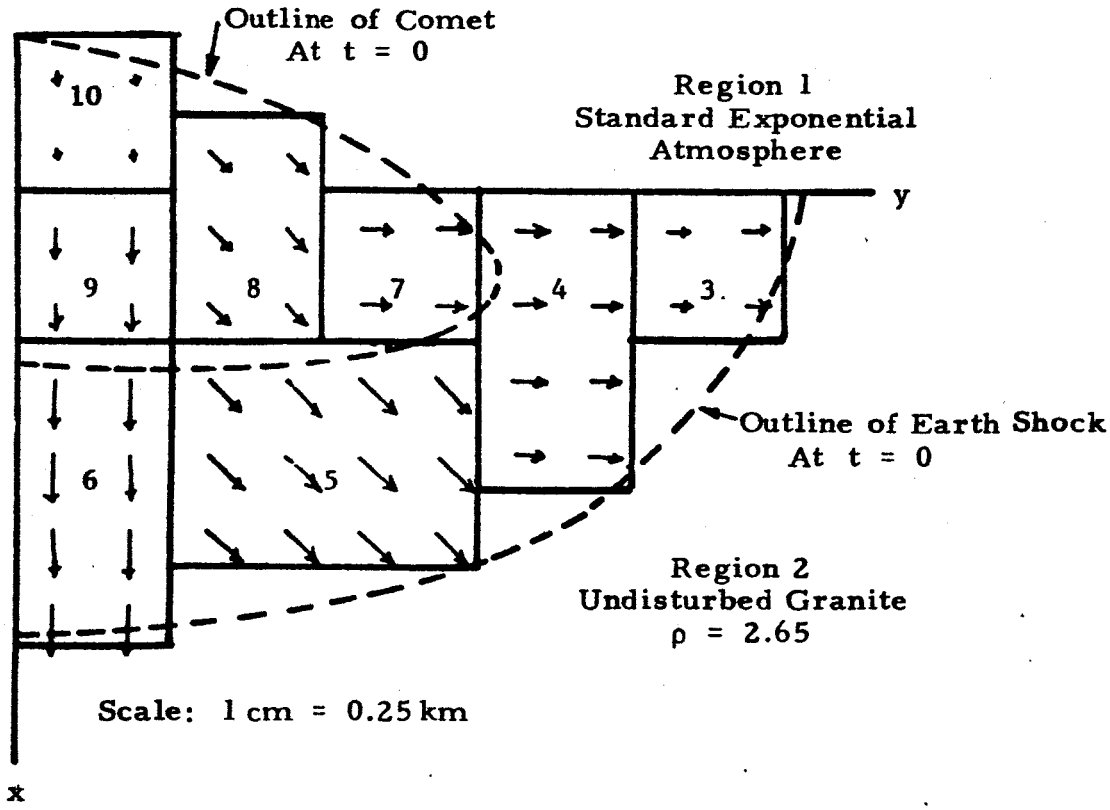

FIGURE 31. INITIAL IMPACT CONFIGURATION FOR COMET, Established by One-Dimensional Code Runs for a 0.216-Density Body Impacting at 30 km/sec

in an Eulerian grid and enhanced by the application of the rezone option, slowed down the expansion velocities of the gas for shallow-angle outgoing trajectories. As a result, only trajectories inclined upward by at least 45 deg were considered in the final analysis.

It was necessary to use the same formulation for the equation of state of air, comet, and earth because of the pure Eulerian grid. Fortunately, this presents no problem. The Tillotson equation of state, described earlier, adapts naturally to this case. The air, comet gas, and vaporized granite had an effective gamma of 1.4, while the liquid and solid material had the principal Hugoniot shown in Figures 24, 25, and 26. A special routine was written into the ELK code to establish an exponentially graded atmosphere, rather than using the constant-density regions described earlier for problems A2, B2, and C2. Gravity was included in this calculation although its effect is negligible in the times of interest. The Von Neuman Q factor was set at zero, and other standard controls were invoked to insure stability. This was done in the expectation of obtaining more accuracy in the calculation. Some oscillation was observed in the expanding velocity field, perhaps attributable to the zero Q, perhaps enhanced by the rezoning option. This is not resolved at present.

A 22 x 32 grid was used, enclosing a cylindrical space with radius 5.5 km. The bottom of this space started at 2.5 km below the earth's surface and extended 5.5 km above. The impacted comet and the shocked earth are defined initially in 50 zones (Figure 31). The ELK rezone option was exercised each time the activity approached the boundary, doubling the linear zone size and conserving the total number of zones. This option was used three times in the course of the calculation, which ended with a grid of radius 44 km, extending to a height of 44 km and a depth of 20 km.

A special computing program, TRACE, was written to follow the trajectories of the expanding gas particles. The time-changing velocity field of the ELK code was used as input to TRACE. Trajectories of 18 select particles were then computed by TRACE. Five typical trajectories are shown in Figure 32. The rezone option was applied at the times

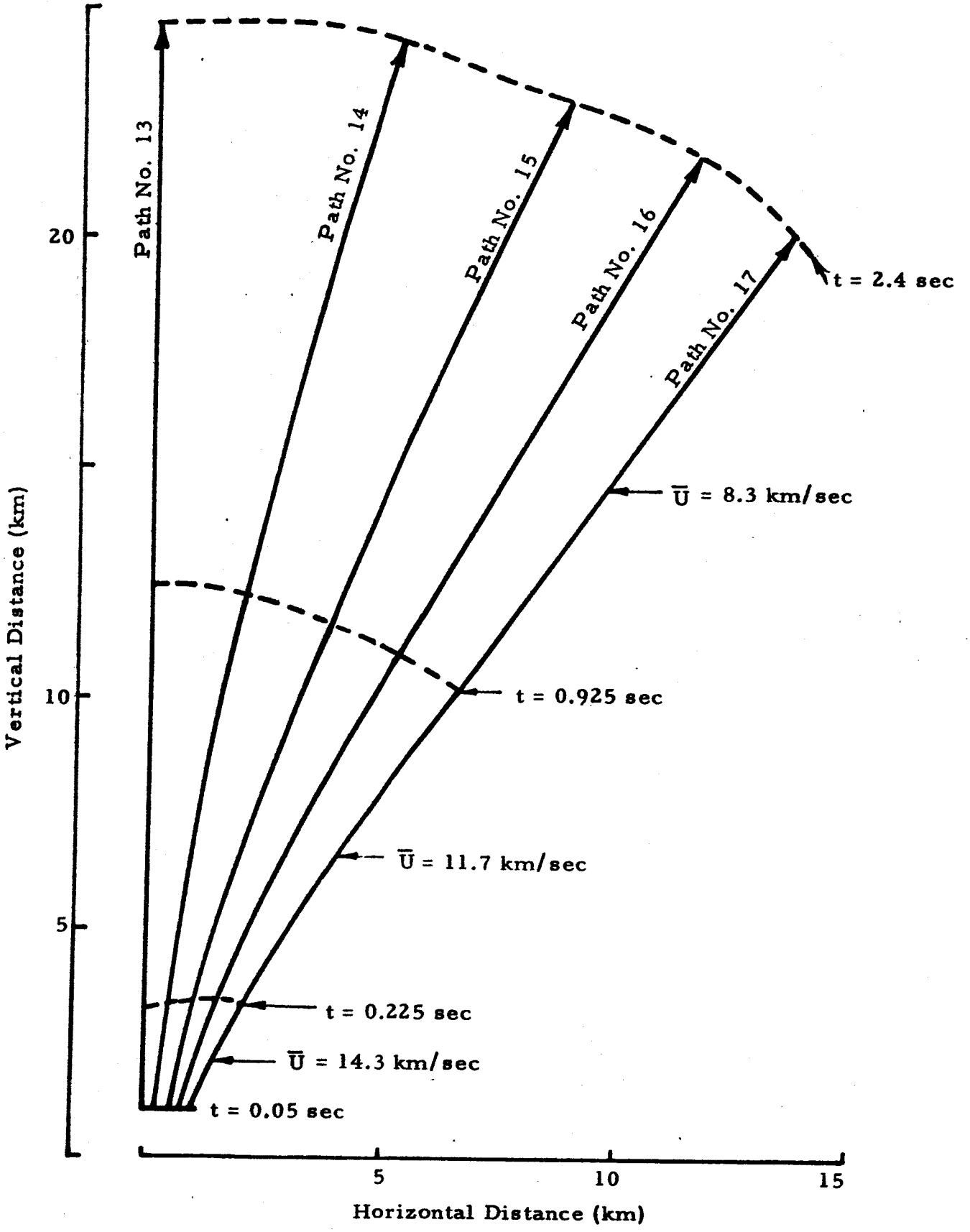

FIGURE 32. TYPICAL TRAJECTORIES FOR PARTICLES COMPUTED BY TRACE

indicated. The mean velocities that apply to these time intervals are shown for Path No. 17. The obvious deceleration makes it impossible for tektite to coast upward keeping a small relative velocity with respect to the gas. Typical densities along these paths are given in the table below.

Typical Densities Along the Paths of Figure 32

Path	t = 0.225 sec	t = 0.925 sec	t = 2.400 sec
13	3.9×10^{-2}	8.2×10^{-4}	1.9×10^{-4}
14	3.9×10^{-2}	8.7×10^{-4}	2.7×10^{-4}
15	3.7×10^{-2}	1.1×10^{-3}	3.8×10^{-4}
16	3.6×10^{-2}	1.6×10^{-3}	4.8×10^{-4}
17	3.6×10^{-2}	1.7×10^{-3}	5.4×10^{-4}

A display of trajectory path in velocity-height space is shown in Figure 33 for a path originating at a 1/2 km height and a 1/2 km radius. The rezone option was applied at times indicated in Figure 32. The path in the velocity-height space shows discontinuities at these times and must be ignored. The dashed line drawn is a section of a "best-guess" path. This severe deceleration is typical of the 18 paths investigated.

4. Conclusions

The calculations presented here refute the model whereby swarms of small molten tektites escape the earth's atmosphere through a general protective blanket of expanding comet gas, resulting from a vertical impact. A truly enormous comet would be required to remove a sector of the atmosphere without serious deceleration of the expanding comet gas. The calculations presented can be refined, but it is unlikely that they are in sufficient error to escape this conclusion. It is not claimed, however, that all mechanisms have been considered. The comet gas expanding preferentially back down a low-density "tunnel" has not been treated. Slanted impacts that could throw up enormous amounts of earth material have not been treated. The possibility of tektite escape through the outgoing tunnels from this material has not been examined. Finally,

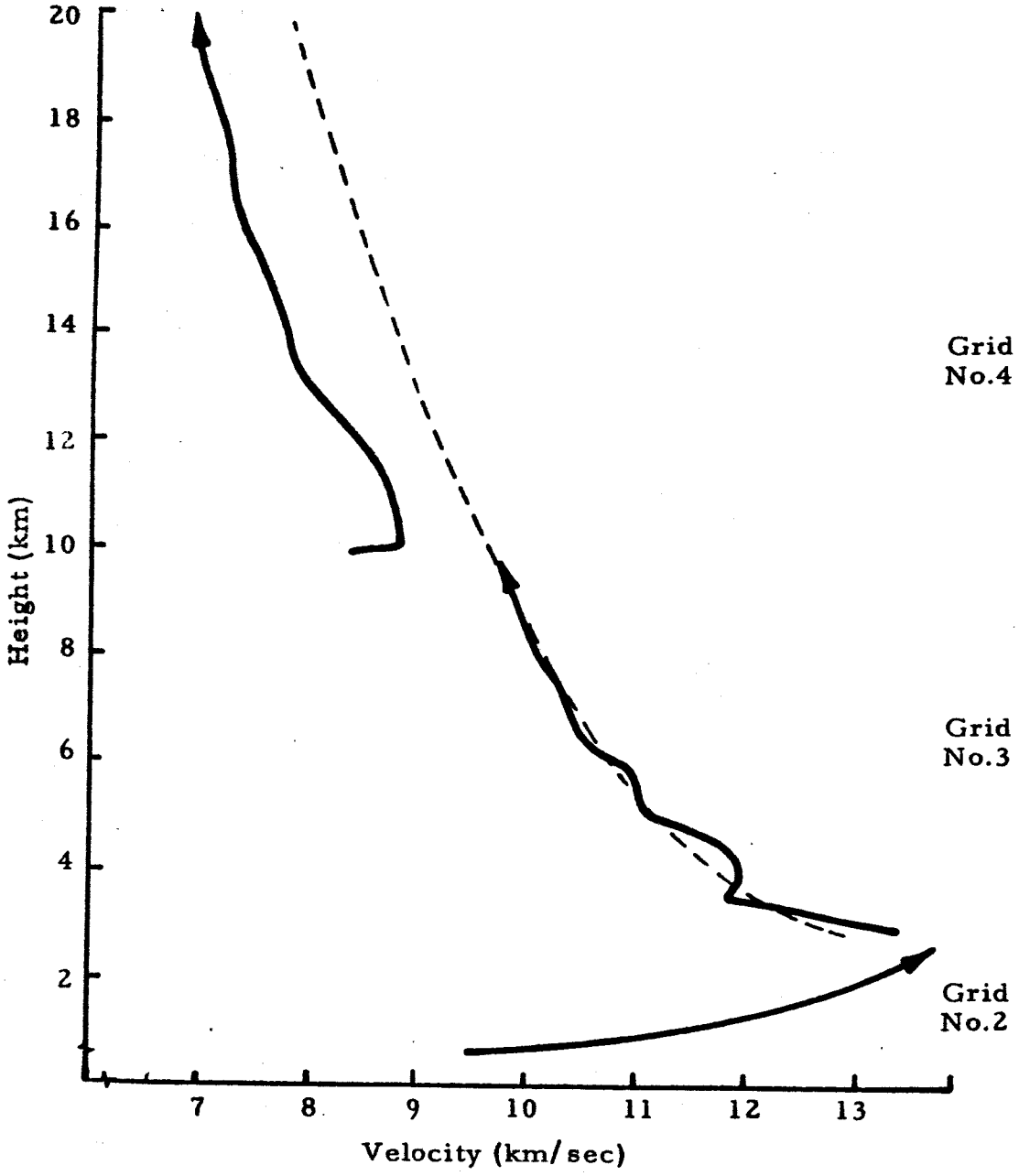

FIGURE 33. VELOCITY AS A FUNCTION OF HEIGHT ON A TYPICAL TRAJECTORY

the conditions for launching more or less intact large parent bodies that could shed tektites have not been established.

The computational methods available could be used to great advantage in studying these mechanisms. The experience gained in performing the present calculations is invaluable. It is felt that a calculation of a slanted impact can be approximated, and that mechanisms for launching large intact masses can be established. It is felt that it is premature to abandon the hypothesis of an earth-comet impact as a possible origin of tektites.

REFERENCES

1. D. J. Andrews, C. S. Godfrey, E. Teatum, and E. T. Trigg, "Calculation of Underground and Surface Explosions," PIFR-013, Physics International Company, November 24, 1965.

2. W. F. Noh, "CEL: A Time-Dependent, Two Space Dimensional, Coupled Eulerian-Lagrange Code," UCRL-7463, University of California Lawrence Radiation Laboratory, August 1963.

3. Physics International Company, "Pressure Vessel Failure Study," PIFR-190, Physics International Company, March 1965.

4. W. E. Johnson, "OIL, A Continuous Two-Dimensional Eulerian Hydrodynamic Code," GAMD-5580, General Atomic, San Diego, California, January 7, 1965.

5. R. C. Bass, H. T. Hawk, and A. J. Chabai, "Hugoniot Data for Some Geologic Materials," SC-4903, Sandia Corporation, Albuquerque, N. Mex., June 1963.

6. V. G. Gregson, T. J. Ahrens, and C. F. Peterson, "Dynamic Properties of Rocks," AFCRL-63-662, Stanford Research Institute, Menlo Park, California, August 1963.

7. R. G. Wuerker, Third Symposium on Rock Mechanics, Quarterly of the Colorado School of Mines 54, 3 (July 1959).

8. T. R. Butkovich, "Calculation of the Shock Wave from an Underground Nuclear Explosion in Granite," UCRL-7763, University of California Lawrence Radiation Laboratory, May 1962.

9. J. Thouvenin, "Action of Shock Waves on Porous Solids," Commissariat a L'Energie Atomique, Paris, France, Translation of a paper given at a Detonation Symposium at Naval Ordnance Laboratory, 1965.

10. G. D. Anderson, Stanford Research Institute, "Equation of State Studies of Porous Earth," paper presented at Ground Shock Calculational Review Meeting at the Rand Corporation, Santa Monica, Calif. October 26-28, 1965.

11. Nicholas M. Short, "Project DANNY BOY, The Definition of True Crater Dimensions by Post-Shot Drilling," WT-1834, Department of Defense, Atomic Energy Commission, July 6, 1964.

12. L. F. Ingram, "Project DANNY BOY, Earth-Motion Measurements," WT-1811, Department of Defense, Atomic Energy Commission, November 20, 1964.

13. J. W. Gehring, C. L. Meyers, and J. A. Charest, "Experimental Studies of Impact Phenomena and Correlation with Theoretical Models," TR-64-66, General Motors Defense Laboratories, Goleta, Calif., December 1964.

14. S. M. Halperson, "Comparison Between Hydrodynamic Theory and Impact Experiments," Proceedings of the Seventh Hypervelocity Impact Symposium, Vol. V, November 7-19, 1964.

15. L. J Spencer, "Origin of Tektites," Nature 132, 571 (1933).

16. L. J. Spencer, "Origin of Tektites," Nature 131, 117-118 (1933).

17. Harold C. Urey, "On the Origin of Tektites," Proc. Natl. Acad. Sci. 41 (1), 27-31 (1955).

18. Harold C. Urey, "The Origin of Tektites," Nature 179, 556-557 (1957).

19. Virgil E. Barnes, "Tektites," Sci. Am. 205 (5), 36, 58-65 (1961).

20. A. J. Cohen, "A Semiquantitative Asteroid Impact Hypothesis of of Tektite Origin" (Abstract), J. Geophys. Res. 66 (8), 2521 (1961).

21. W. Gentner, H. J. Lippolt, and O. A. Schaeffer, "Kalium-Argon-Alter der Gläser des Nördlinger Rieses Und der Böhmischmährischer Tecktite," Max-Plank-Inst. Kernphysik Rept. (1962).

22. D. R. Chapman, and H. K. Larson, J. Geophys. Res. 68 (14), (1963).

23. D. R. Chapman, "An Analysis of Base Pressure at Supersonic Velocities and Comparison with Experiment," National Aeronautics and Space Administration Technical Report No. 1051. (1951).

24. C. S. Godfrey, D. J. Andrews, and E. T. Trigg, "Study of Two-Dimensional Calculation of Cratering," PIFR-101A, Physics International Company, 1965.

APPENDIX A

DERIVATION OF BULK AND SHEAR MODULI FROM ISOTROPIC ASSUMPTIONS

It may be shown that for an isotropic solid the generalized form of Hooke's law becomes

$$\begin{aligned} \sigma_x &= 2\mu\epsilon_x + \lambda\Delta \\ \sigma_y &= 2\mu\epsilon_y + \lambda\Delta \\ \sigma_z &= 2\mu\epsilon_z + \lambda\Delta \end{aligned} \tag{1}$$

$$\tau_{xy} = \mu\gamma_{xy}, \quad \tau_{yz} = \mu\gamma_{yz}, \quad \tau_{zx} = \mu\gamma_{zx}$$

where σ_x, σ_y, and σ_z are the normal stresses in the x, y, and z directions, respectively; ϵ_x, ϵ_y, and ϵ_z are the normal strains corresponding to σ_x, σ_y, and σ_z; τ_{xy}, τ_{yz}, and τ_{zx} are the shearing stresses in the direction of the first subscript acting in a plane perpendicular to the direction of the second subscript; γ_{xy}, γ_{yz}, and γ_{zx} are the shearing strains corresponding to τ_{xy}, τ_{yz}, and τ_{zx}; λ and μ are the Lamé parameters; and $\Delta \equiv \epsilon_x + \epsilon_y + \epsilon_z$, the volumetric strain. The shear modulus (i.e., the material property that relates shear stress to shear strain) is nothing more than the Lamé parameter μ, while the bulk modulus k (i.e., the material property which relates normal stress to normal strain) is found by considering an equal triaxial compression

$$\sigma_x = \sigma_y = \sigma_z = -P, \quad \tau_{xy} = \tau_{yz} = \tau_{zx} = 0 \tag{2}$$

Substituting these conditions into the set of equations (1) yields $k \equiv P/\Delta = \lambda + \frac{2}{3}\mu$, or more meaningfully $\lambda = k - \frac{2}{3}\mu$. Equation (1) may now be rewritten as

$$\begin{aligned} \sigma_x &= 2\mu\epsilon_x + \Delta\,(k - \tfrac{2}{3}\mu) \\ \sigma_y &= 2\mu\epsilon_y + \Delta\,(k - \tfrac{2}{3}\mu) \end{aligned} \tag{3}$$

$$\sigma_z = 2\mu\epsilon_z + \Delta\,(k - \tfrac{2}{3}\mu) \qquad (3)\ \text{(cont'd)}$$

$$\tau_{xy} = \mu\gamma_{xy},\quad \tau_{yz} = \mu\gamma_{yz},\quad \tau_{zx} = \mu\gamma_{zx}$$

The set of equations (3) constitute the stress-strain relationships of an isotropic medium.

Applying these relations to the equations of motion, it can be shown that for the case of pure shear, $\epsilon_x = \epsilon_y = \epsilon_z = 0$, i.e., $\Delta = 0$, a wave equation of the form

$$\rho\frac{\partial^2\bar{\omega}}{\partial t^2} = \mu\nabla^2\bar{\omega} \qquad (4)$$

is achieved where $\bar{\omega}$ is the rotation due to shear. From this it is seen that the transverse- or shear-wave speed is

$$c_t = \sqrt{\frac{\mu}{\rho}} \qquad (5)$$

$$\mu = c_t^2\rho \qquad (5a)$$

For the case of pure compression $\gamma_{xy} = \gamma_{yz} = \gamma_{zx} = 0$, i.e., $\bar{\omega} = 0$, the analogous relation is

$$\rho\frac{\partial^2\Delta}{\partial t^2} = (k + \tfrac{4}{3}\mu)\,\nabla^2\Delta \qquad (6)$$

Hence the logitudinal- or compression-wave speed is

$$c_\ell = \sqrt{\frac{k + \frac{4}{3}\mu}{\rho}} \qquad (7)$$

$$k = c_\ell^2\rho - \tfrac{4}{3}\mu \qquad (7a)$$

APPENDIX B

DERIVATION OF LOADING CURVE FOR LOOSE BASALT COMPACTION MODEL

In order to determine the bulk modulus of loose basalt, it was assumed that the sound speed of 1.85 g/cm^3 basalt was comparable to 1.85 g/cm^3 tuff. Therefore, since 1.85 g/cm^3 tuff has a longitudinal sound speed of 0.21 cm/μsec and 2.62 g/cm^3 basalt has a longitudinal sound speed of 0.45 cm/μsec, the following relation was written for the longitudinal sound speed of 2.25 g/cm^3 basalt.

$$c_\ell = \frac{2.25 - 1.85}{2.62 - 1.85} \times (0.45 - 0.21) + 0.21$$

$$c_\ell = 0.125 + 0.21 = 0.335 \text{ cm/μsec}$$

The transverse sound speed was derived by using the relationship that $c_\ell/c_t = \sqrt{3}$, and hence $c_t = 0.1935$ cm/μsec. Equations 5a and 7a from Appendix A could now be applied, yielding the shear and bulk moduli

$$\mu = (0.1935)^2 (2.25) = 0.084$$

$$k = (0.335)^2 (2.25) - \frac{4}{3}(0.084) = 0.1415$$

and finally assuming the loading path to be linear, the equation of state $P = 0.1415\mu$ resulted.